

Bing Han

INFLUENCE OF MULTI-PHASE PHENOMENA ON SEMIBATCH CRYSTALLIZATION PROCESSES OF AQUEOUS SOLUTIONS

Thesis for the degree of Doctor of Science (Technology) to be presented with due permission for public examination and criticism in the Auditorium 1382 at Lappeenranta University of Technology, Lappeenranta, Finland on the 7th of August, 2015, at noon.

Acta Universitatis
Lappeenrantaensis 646

Supervisors	Professor Marjatta Louhi-Kultanen School of Engineering Science Lappeenranta University of Technology Finland
	Professor Harri Niemi School of Engineering Science Lappeenranta University of Technology Finland
	Professor Zuoliang Sha College of Marine Science & Engineering Tianjin University of Science & Technology China
Reviewers	Professor Dr. Heike Lorenz Max Planck Institute for Dynamics of Complex Technical Systems Germany
	Professor David Hongyuan Wei School of Chemical Engineering Tianjin University China
Opponents	Professor Dr. Heike Lorenz Max Planck Institute for Dynamics of Complex Technical Systems Germany
	Professor Jens-Petter Andreassen Department of Chemical Engineering Norwegian University of Science and Technology Norway
Custos	Professor Marjatta Louhi-Kultanen School of Engineering Science Lappeenranta University of Technology Finland

ISBN 978-952-265-813-5
ISBN 978-952-265-814-2 (PDF)
ISSN-L 1456-4491
ISSN 1456-4491

Lappeenranta teknillinen yliopisto
Yliopistopaino 2015

ABSTRACT

Bing Han

Influence of multi-phase phenomena on semibatch crystallization processes of aqueous solutions

Lappeenranta 2015

73 p.

Acta Universitatis Lappeenrantaensis 646

Diss. Lappeenranta University of Technology

ISBN 978-952-265-813-5, ISBN 978-952-265-814-2 (PDF),

ISSN-L 1456-4491, ISSN 1456-4491

Crystal properties, product quality and particle size are determined by the operating conditions in the crystallization process. Thus, in order to obtain desired end-products, the crystallization process should be effectively controlled based on reliable kinetic information, which can be provided by powerful analytical tools such as Raman spectrometry and thermal analysis. The present research work studied various crystallization processes such as reactive crystallization, precipitation with anti-solvent and evaporation crystallization. The goal of the work was to understand more comprehensively the fundamentals, phenomena and utilizations of crystallization, and establish proper methods to control particle size distribution, especially for three phase gas-liquid-solid crystallization systems.

As a part of the solid-liquid equilibrium studies in this work, prediction of KCl solubility in a $\text{MgCl}_2\text{-KCl-H}_2\text{O}$ system was studied theoretically. Additionally, a solubility prediction model by Pitzer thermodynamic model was investigated based on solubility measurements of potassium dihydrogen phosphate with the presence of non-electronic organic substances in aqueous solutions. The prediction model helps to extend literature data and offers an easy and economical way to choose solvent for anti-solvent precipitation.

Using experimental and modern analytical methods, precipitation kinetics and mass transfer in reactive crystallization of magnesium carbonate hydrates with magnesium hydroxide slurry and CO_2 gas were systematically investigated. The obtained results gave deeper insight into gas-liquid-solid interactions and the mechanisms of this heterogeneous crystallization process. The research approach developed can provide theoretical guidance and act as a useful reference to promote development of gas-liquid reactive crystallization.

Gas-liquid mass transfer of absorption in the presence of solid particles in a stirred tank was investigated in order to gain understanding of how different-sized particles interact with gas bubbles. Based on obtained volumetric mass transfer coefficient values, it was found that the influence of the presence of small particles on gas-liquid mass transfer cannot be ignored since there are interactions between bubbles and particles.

Raman spectrometry was successfully applied for liquid and solids analysis in semi-batch anti-solvent precipitation and evaporation crystallization. Real-time information such as supersaturation, formation of precipitates and identification of crystal polymorphs could be obtained by Raman spectrometry.

The solubility prediction models, monitoring methods for precipitation and empirical model for absorption developed in this study together with the methodologies used gives valuable information for aspects of industrial crystallization. Furthermore, Raman analysis was seen to be a potential controlling method for various crystallization processes.

Keywords: absorption of CO₂, dissolution, evaporation crystallization, Pitzer model, precipitation with anti-solvent, Raman spectrometry, reactive crystallization, reaction kinetics, solid-liquid equilibrium

ACKNOWLEDGEMENTS

This study was carried out in the Thermal Unit Operations research group of the Laboratory of Separation Technology at Lappeenranta University of Technology and Tianjin Key Laboratory of Marine Science and Chemistry at Tianjin University of Science & Technology.

First and foremost, I would like to express my deepest gratitude to my supervisors, Prof. Marjatta Louhi-Kultanen and Prof. Zuoliang Sha, for giving me the opportunity to do this work, for their professional guidance, and for their constant encouragement and support during the past years. Special thanks go to D.Sc. Harri Niemi for his expert guidance and our valuable discussions on mass transfer.

I am also grateful to Associate Prof. Haiyan Qu for offering me the chance to do analysis work in the Institute of Chemical Engineering, Biotechnology and Environmental Technology, University of Southern Denmark. Her invaluable suggestions greatly helped in investigation of Raman spectrometry and thermal analysis methods.

I would like to express my gratitude to all the staff working at LUT Chemical Technology for their assistance, collaboration and support. Mr. Markku Maijanen is thanked for his kind help with the experimental set-ups. Master of Science students Sung-ah Kang, Ferran Esteve Pijuan, Muhammad Maan, Hafiz Maan and Rasmus Peltola are acknowledged for their help with the experiments and analysis of my research work.

I am appreciative of the work of Mr. Peter G. Jones with the language of the manuscripts and summary part of the thesis. He gave me valuable comments to improve the quality of the manuscripts.

I also would like to express my gratitude to my friends, Iris Panorel, Wenli Zhao, Mei Han, Yongbo Wang, Ming Li, Waroonkarn Srithammavut and Johanna Puranen for all their help and support.

I would like to acknowledge the Centre for International Mobility CIMO, LUT Foundation of Chemistry and Mathematics, Academy of Finland, Tekes, Centre for Separation Technology and the National Science Foundation of China for financial support of my research.

Last but not least, I want to thank my husband, Xing Shi, for his encouragement, understanding and companionship throughout this work. My daughter, Yuhan Shi, is thanked for her lovely smile, which can always encourage me to do better. Their love and support give me enormous power and courage. My warmest gratitude goes to my parents, Zili Han and Chunying Liu, and my sister, Rong Han, in China for their love and kind support over all the years.

Bing Han
August 2015 Lappeenranta, Finland

Contents

Abstract

Acknowledgements

Contents

List of Publications	9
List of Symbols and Abbreviations	11
PART I: Overview of the Thesis	13
1. Introduction.....	15
1.1 Background	15
1.2 Objective and scope of the work	16
2. Solubility modeling of crystallizing compounds in solutions	18
2.1 Introduction	18
2.2 Pitzer thermodynamic theory	18
2.2.1 Activity coefficient for pure electrolyte solution	19
2.2.2 Activity coefficient for mixed electrolytes	20
2.3 Solubility prediction of potassium chloride in a $\text{MgCl}_2\text{-KCl-H}_2\text{O}$ system.....	22
2.4 Solubility of potassium dihydrogen phosphate in aqueous solutions containing non-electrolyte organic compounds (Publication II)	23
2.4.1 Experimental section.....	23
2.4.2 Results and discussion	23
2.5 Summary	25
3. Reactive crystallization of magnesium carbonate	26
3.1 Magnesium carbonate precipitates	26
3.1.1 Formation of magnesium carbonates	26
3.1.2 Production of magnesium carbonate by homogeneous liquid reaction	26
3.1.3 Production of magnesium carbonate by heterogeneous gas-liquid reaction	27
3.2 Factors impacting the particle size distribution of magnesium carbonate	27
3.2.1 Experimental part	27
3.2.2 Results and discussion	28
3.3 Precipitation kinetics of magnesium carbonate	33
3.3.1 Experimental section.....	33
3.3.2 Effect of CO_2 flow rate (Publications IV and V)	35
3.3.3 Effect of stirring speed (Publications IV and V)	35
3.3.4 Characteristics of the crystallized product (Publication V)	35

3.4	Carbonation process monitored by in-line Raman spectroscopy	36
3.4.1	Experimental section.....	36
3.4.2	Results and discussion	38
3.5	Summary	39
4.	Mass transfer of absorption in the presence of suspended solid particles in a stirred tank.....	40
4.1	Introduction	40
4.1.1	Mechanism of mass transfer of absorption at gas-liquid interfaces	40
4.1.2	Effect of solids on the mechanism of mass transfer of absorption.....	40
4.1.3	Factors affecting mass transfer of absorption	41
4.2	Experimental section.....	42
4.2.1	Experimental material.....	42
4.2.2	Experimental method.....	43
4.3	Results and discussion	47
4.3.1	Absorption of oxygen to water in an air-water system.....	47
4.3.2	Influence of quartz particles on absorption mass transfer of oxygen in an air-water system.....	48
4.3.3	Influence of calcium carbonate particles on the absorption mass transfer of oxygen in an air-water system	49
4.3.4	Gas-liquid mass transfer model in the presence of solids.....	50
4.4	Summary	51
5.	Application of Raman spectrometry to anti-solvent precipitation and evaporation crystallization	53
5.1	Anti-solvent precipitation of potassium dihydrogen phosphate (Publication I)	53
5.1.1	Introduction	53
5.1.2	Experimental section.....	54
5.1.3	Results and discussion	54
5.2	Evaporation crystallization of indomethacin solutions (Publication III).....	58
5.2.1	Experimental section.....	58
5.2.2	Results and discussion	59
5.3	Summary	59
6.	Conclusions.....	60
	References	63
	Appendix A.....	70
	PART II: Publications	73

List of publications

This thesis is based on the following papers, which are referred to in the text by Roman numbers I-V.

- I. Han B., Sha Z., Qu H., Louhi-Kultanen M., Wang X. (2009). Application of on-line Raman spectroscopy on monitoring semi-batch anti-solvent crystallization, *CrystEngComm*, **11**(5), pp. 827-831.
- II. Han B., Sha Z., Partanen J., Louhi-Kultanen M. (2012). Solubility of potassium dihydrogen phosphate in aqueous solutions of acetone, ethyl acetate, and thiourea from $T = (298.15\text{--}313.15)$ K, *Fluid Phase Equilibria*, **336**, pp. 16-21.
- III. Hellstén S., Han B., Mäkilä E., Niemi H., Salonen J., Lehto V.-P., Stelzer T., Louhi-Kultanen M., Ulrich J. (2013). Insights into the evaporation kinetics of indomethacin solutions, *Chemical Engineering & Technology*, **36**(8), pp. 1300-1306.
- IV. Han B., Qu H., Niemi H., Sha Z., Louhi-Kultanen M. (2014). Mass transfer and kinetics study of heterogeneous semi-batch precipitation of magnesium carbonate, *Chemical Engineering & Technology*, **37**(8), pp. 1363-1368.
- V. Han B., Qu H., Niemi H., Sha Z., Louhi-Kultanen M. (2014). Mechanistic study of magnesium carbonate semibatch reactive crystallization with magnesium hydroxide and CO₂, *Ind. Eng. Chem. Res.*, **53**(30), pp. 12077-12082.

Contribution of the author

The author planned and carried out all experiments, made the calculations, established the calibration of Raman spectroscopy, and explained the results for Publications I, II, IV and V. The author wrote the manuscripts together with the other co-authors.

The author carried out analysis by Raman spectroscopy and did some parts of the evaporation experiments in Publication III. Moreover, the author wrote the manuscript partly with the other co-authors.

Associated publications:

- I. Han B., Niemi H., Sha Z., Louhi-Kultanen M. (2011). Influence of solid particles on gas-liquid mass transfer in stirred tank. *18th International Symposium on Industrial Crystallization*, Zurich, Switzerland, 13-16, September. *Poster presentation*.
- II. Han B., Niemi H., Sha Z., Louhi-Kultanen M. (2012). Precipitation of magnesium carbonate by a reaction of magnesium hydroxide and CO₂. *19th International Workshop on Industrial Crystallization*, Tianjin, China, 7-9 September. *Oral presentation*.
- III. Niemi H., Han B., Louhi-Kultanen M. (2012). Evaporation crystallization study with organic compounds. *HANBAT International Workshop on Industrial and*

- Pharmaceutical Crystallization*, Deajeon, Korea, 3-5, September. *Poster presentation*.
- IV. Han B., Niemi H., Sha Z., Louhi-Kultanen M. (2013). Precipitation kinetics of magnesium carbonate hydrates measured by Raman spectroscopy. *20th International Workshop on Industrial Crystallization*, Odense, Denmark, 18-20 September. *Oral presentation*.
- V. Han B., Sha Z., Louhi-Kultanen M. (2014). Study on impacts of magnesium carbonate trihydrate particle size distribution. *Journal of Tianjin University of Science & Technology*, 29(2), pp. 45-49. (in Chinese)
- VI. Han B., Deshayes L., Louhi-Kultanen M. (2014). Process monitoring of carbonate precipitation by in-line Raman spectroscopy. *Joint Congress of Asian Crystallization Technology Symposium-2014 and 11th International Workshop on Crystal Growth of Organic Materials*, Nara, Japan, 17-20, June. *Poster presentation*.
- VII. Puranen J., Niemi H., Han B., Louhi-Kultanen M. (2014). Evaporation rates of pure solvents and carbamazepine solutions. *19th International Symposium on Industrial Crystallization*, Toulouse, France, 16-19, September. *Poster presentation*.
- VIII. Louhi-Kultanen M., Han B., Nurkka A., Hatakka H. (2015). An undergraduate laboratory exercise for studying kinetics of batch crystallization. *Chemical Engineering Education*, accepted.
- IX. Sha Z., Han B., Louhi-Kultanen M. (2015). Influence of solid particles on gas-liquid mass transfer in a stirred tank. *Journal of Tianjin University of Science & Technology*, accepted. (in Chinese)

List of symbols and abbreviations

Symbols

A^ϕ	Debye-Hückel coefficient ($(\text{mol kg}^{-1})^{-1/2}$)
a	gas-liquid interfacial area (m^2)
B	coefficient in the second virial, related to ion strength (kg mol^{-1})
B'	ion strength differential of B
B_{MX}'	function of ion strength (kg mol^{-1})
b_p	empirical constant, equal to $1.2 (\text{mol kg}^{-1})^{-1/2}$
C	concentration of oxygen in liquid (mg L^{-1})
C_0	oxygen concentration at $t = 0$ (mg L^{-1})
C^*	oxygen solubility (mg L^{-1})
C_{MX}'	function of C_{MX}^Φ (kg mol^{-2})
C_{MX}^Φ	Pitzer constant (kg mol^{-2})
D	diameter of impeller (m)
d_p	average particle diameter (m)
f^γ	function of ion strength
g	gravity acceleration (m s^{-2})
I_m	ionic strength of solution (mol kg^{-1})
$J(x)$	group integration for short-range interaction potential energy
$J'(x)$	first order derivative of $J(x)$
k_L	gas-liquid mass transfer coefficient (m s^{-1})
$k_L a$	volumetric mass transfer coefficient (s^{-1})
m	molality (mol kg^{-1})
N_c	specie number of cation
N_{js}	critical impeller speed for solids (rpm)
N_{jsg}	critical impeller speed for gas-liquid-solid system (rpm)
P_G	power input (W)
Q_V	ratio of gas flow rate to liquid volume ($\text{m}^3 \text{ m}^{-3} \text{ min}^{-1}$)
S	impeller constant
T	temperature (K)
t	time (s)
u_g	superficial gas velocity (m s^{-1})
v	ion number
V_L	liquid volume (m^3)
w_s	solid mass fraction (%)
X	mass ratio of suspended solids to liquid $\times 100$ ($\text{kg solid/kg liquid} \times 100$)
Z	charge number

Greek symbols

α, β, κ	empirical parameter, eq. 4.4
-------------------------	------------------------------

$\beta_{MX}^{(0)}, \beta_{MX}^{(1)}, \beta_{MX}^{(2)}$	Pitzer parameters (kg mol^{-1})
γ	activity coefficient
ε_s	solid volume fraction (%)
$^E\theta_{ij}$	charge number of i and j ions (kg mol^{-1})
$^E\theta'_{ij}$	function of ion strength I_m
λ	ion-molecule interaction parameter
μ^*	effective viscosity of the particle-liquid mixture ($\text{kg m}^{-1} \text{s}^{-1}$)
μ_L	viscosity of the liquid ($\text{kg m}^{-1} \text{s}^{-1}$)
ν	kinematic viscosity ($\text{m}^2 \text{s}^{-1}$), eq. 4.1
ρ	liquid density (kg m^{-3})
ρ_p	particle density (kg m^{-3})
τ	response time of oxygen probe (s)
Ψ	interactions of three different ions ($\text{kg}^2 \text{mol}^{-2}$)
Φ	Pitzer interaction of co-ion (two cations or two anions) ($\text{kg}^2 \text{mol}^{-2}$)

Superscripts and subscripts

A, A'	anion
C, C'	cation
G	gas
L, l	liquid
M	cation
N	neutral
X	anion
\pm	average

Abbreviations

KDP	KH_2PO_4
IMC	indomethacin
XRD	X-ray powder diffraction

PART I: Overview of the Thesis

1. Introduction

1.1 Background

Compared with other separation technologies for chemicals, crystallization offers many advantages, such as moderate operating conditions, high purity of product and low costs. Depending on the specific system and properties of the compounds involved, different crystallization methods such as cooling crystallization, evaporation crystallization, melt crystallization, precipitation methods based on using anti-solvents, or reactive crystallization can be chosen. However, desired product with uniform particles and specific crystalline shape can only be produced under optimized operating conditions. Most crystallization methods aim to reduce the solubility of the crystallization compound by temperature or solution composition changes or by chemical reactions. Therefore, knowledge of the solubility is essential for the design and control of crystallization processes. Consequently, there is a need to develop solubility predictions which require only a small amount of experimental data and which can predict with the aid of different thermodynamic models the solubility of substances in different solvents over a wide range of conditions.

Reactive crystallization is a core technology in industrial crystallization. It is a reaction process in either gas-liquid or liquid-liquid phases to produce poorly soluble substances (Ding 1985). Reactive crystallization can be used for separating and purifying substances that are easily precipitated from solutions containing also other compounds. Reactive crystallization can be considered as a complex process because it includes two processes; namely, the chemical reactions occurring between the reactants and the precipitation itself. The rates of the chemical reactions and crystallization are crucial factors controlling the particle size distribution. Moreover, macro- and micro-scale mixing is also important for the properties of the final product.

In the last decades, reactive crystallization research has mainly focused on homogeneous liquid-liquid systems in which the reactants are dissolved. Several studies have reported the effect of mixing on the reaction rate and crystallization rate and have concluded that the reaction rate is an important parameter for controlling the crystallization and the precipitates formed. Most precipitates formed from fast reactions are usually sparingly soluble. Thus, supersaturation increases significantly due to the fast occurrence of preliminary nucleation, which leads to the formation of fine particles. The reaction rate is mainly controlled by adjusting the mixing time of the reactants in the reactor. Therefore, hydrodynamics in the reactor plays a crucial role for understanding reactive crystallization. Reactive crystallization has nowadays found many applications, such as preparation of ultrafine particles, catalysts, magnetic materials, electronic ceramic materials, dispersants, pigments and auxiliaries (Stankiewicz 2003, Tosheva and Valtchev 2005, Purxins et al. 2006, Carteret et al. 2009). With the development of technology, gas-liquid reactive crystallization is evolving and is now finding application in areas such as the preparation of nanomaterials, synthetic products, petrochemicals, and

polymer materials. (Sun et al. 2013, Chen et al. 2004, Varma et al. 2011, Nandi et al. 2014)

In gas-liquid reactive crystallization, the reactions between the gas and liquid are more complex than the homogeneous reactions occurring in a single liquid phase, due to the contribution of the gaseous reactant. At the same time, a new solid phase occurs by crystallization. Therefore, the whole system contains three phases, i.e. gas-liquid-solid. This multi-phase system includes gas-liquid mass transfer, reaction and crystallization from the supersaturated mother liquor to the solid phase. In such systems, gas-liquid mass transfer kinetics, reaction kinetics and crystallization kinetics affect the properties of the final product. Moreover, the mass transfer kinetics between the gas and liquid phases is affected by many factors, such as gas hold-up and bubble size distribution.

Bubble appearance in the reactor is related to the gas properties, liquid properties and fluid hydrodynamics. The interactions between the bubbles and particles have a crucial impact on the system, and these interactions affect the kinetics of mass transfer and further crystallization kinetics. Therefore, gas bubble behavior in the dynamic system plays an important role in reactive crystallization.

Most researchers have investigated the selection of reaction equipment, scale-up, optimum operating conditions and the improvement of production capacity from a practical perspective. Study of reaction kinetics, crystallization kinetics and interaction mechanisms in gas-liquid reaction crystallization is less prevalent. Due to the considerable number of impacting factors and the complex process, different kinetic models and equations have been obtained for specific systems by different researchers using different methods.

Inline information such as concentration of substance, supersaturation, and the quantities of precipitated crystals is useful in understanding of the mechanisms of crystallization. However, obtaining such real-time information is difficult for both the reaction and the crystallization since the processes are relatively fast. Advanced techniques, however, exhibit potential for capturing inline information, enabling the real changes during the process to be identified, which would be valuable for further development of industrial crystallization.

1.2 Objective and scope of the work

In the present work, various crystallization processes such as reactive crystallization, precipitation with anti-solvent and evaporation crystallization were investigated in semibatch mode. The aim was to understand the mechanisms of these crystallization processes and to establish methods to control the crystal size distribution in gas-liquid reaction crystallization. In the gas-liquid reactive crystallization under study, slurries containing solid reactant particles were used as reactant solutions. Consequently, solids are present in the whole process. This heterogeneous reaction is complicated due to dissolution of the reactant and its kinetics differs from a homogeneous reaction where the

reactant is fully dissolved in the solution. Moreover, several steps such as absorption of gas into liquid phase, dissolution of reactant, chemical reactions and precipitation occur simultaneously in the studied gas-liquid reactive crystallization. These steps are considerable difficult to investigate at the same time since they happen so fast. Therefore, various chemical processes such as absorption, the influence of inert particles on absorption, and precipitation were studied separately. Conventional crystallization kinetics methods of nucleation and crystal growth rate based on crystal size distribution analysis cannot be used for such heterogeneous systems because the crystal size distribution analysis would yield results in which the fraction of reactant particles cannot be distinguished. Therefore, accurate nucleation or crystal growth cannot be obtained. The kinetics study in the current work is thus based on solid phase composition analyses. Solid composition monitoring gives crucial data on solid reactant dissolution and formation of precipitate.

A further objective was also to stimulate novel and innovative ideas for the application of other complex gas-liquid reactive crystallizations. Raman spectrometry, as a modern analytical tool, can be applied for analysis of these crystallization processes. It can provide inline or offline information to identify the crystal polymorphs and to study crystallization kinetics and mechanisms. Simultaneous use of a laser diffraction size analyzer and thermal analyzer can enable kinetic data to be obtained, allowing study of the reaction mechanism and fundamentals of gas-liquid reactive crystallization. Furthermore, Pitzer thermodynamics modeling can provide appropriate tools for solubility predictions of a solute in the presence of various admixtures.

The thesis consists of theoretical and experimental parts. The Pitzer thermodynamic model is introduced in detail in Chapter 2. Application of the Pitzer model in solubility prediction of KCl in an $\text{MgCl}_2\text{-KCl-H}_2\text{O}$ system and of KH_2PO_4 in non-electrolyte solutions was studied. The results of the latter were presented in Publication II. The results presented in Publications IV and V concerning mass transfer and kinetics of magnesium carbonate semi-batch reactive crystallization with magnesium hydroxide and carbon dioxide are explained and summarized in Chapter 3. Chapter 4 discusses the mass transfer of absorption in the presence of suspended solid particles in a stirred tank. Application of Raman spectrometry in anti-solvent precipitation of KH_2PO_4 from binary solvents and evaporation crystallization of indomethacin from organic solvents is summarized in Chapter 5. The results were mainly presented in Publications I and III. The conclusions of the present study and the outlook for future work are summarized in Chapter 6.

2. Solubility modeling of crystallizing compounds in solutions

2.1 Introduction

Crystallization or precipitation can efficiently separate solute compounds in solid form. The solubility of the crystallizing compound in the solution is the key factor for the crystallization. Solubility is a measurement of the dissolution capacity of the solvent, i.e. the amount of solute dissolved in a unit volume of solvent at a certain temperature. Thus, solubility affects the selection of the crystallization method (evaporation, cooling, etc.) used to generate supersaturation in the solution to a large extent. The solubility is an indispensable part of crystallization operations and it is affected by many factors, such as temperature, solution composition and pressure.

Although solubility data of many pure substances are available in databases or reported in literature, the fast pace of developments in chemical technology often results in a need for solubility data for a new compound or new solvent. Moreover, obtaining solubility data from extensive experimental investigations can be time-consuming and costly, and material consumption can be significant. Consequently, current research is increasingly focusing on predicting solubility of different systems based models such as the Pitzer model, for aqueous solutions, and UNIQUAC, Wilson and NRTL models for organic compound systems (Kuramochi et al. 2005, Jouyban et al. 2002, Pinho et al. 2002). If a theoretical solubility model can be applied for the specific compound system, a relatively small amount of experimental data is usually required for data fitting.

2.2 Pitzer thermodynamic theory

In precipitation or crystallization processes, description of the thermodynamic equilibrium for the solid-liquid phases is a crucial step when the solutions are not ideal. Activity coefficients can be used for prediction of how the admixtures present in the solution or how anti-solvents affect the solubility of the crystallizing compound. For highly non-ideal solutions, the driving force when expressed by concentration differences or concentration ratios between supersaturated solution and the solution at equilibrium can have insufficient accuracy, and activity coefficients are required in such cases as well. The present work focuses on solubility modeling of aqueous solutions based on Pitzer theory, which gives a way to calculate ion activity coefficient and osmotic coefficient of solvent.

The activity coefficient expresses a basic property of an electrolyte solution and is important for solubility prediction of inorganic salts, liquid-liquid extraction, and salt water phase diagram calculation. The activity coefficient of the electrolyte in a certain range of temperatures and solution compositions can be determined by thermodynamic models.

Thermodynamics of electrolyte solubility is the description of a non-ideal solution by calculating its activity coefficient. In the 1970s, Pitzer (1973a, 1973b) extended Debye-Hückel electrolyte theory to concentrated solutions, forming Pitzer theory. The core of this theory is a semi-empirical equation for calculating ion activity coefficient and solvent osmotic coefficient.

Pitzer theory can be applied for thermodynamics modeling of many compound systems, such as pure and mixed electrolyte solutions, symmetric and non-symmetric electrolytes, inorganic and organic electrolytes, dissociate equilibria of electrolytes and neutral molecules. It can also be used for the calculation of thermodynamic properties under high temperature and pressure at molten salt conditions (Niu et al, 2001).

2.2.1 Activity coefficient for pure electrolyte solution

For pure electrolyte MX with the molality m , mean activity coefficient can be expressed as (Pitzer 1991):

$$\ln \gamma_{\pm MX} = |z_M z_X| f^\gamma + \left(\frac{2\nu_M \cdot \nu_X}{\nu} \right) m \cdot B_{MX}^\gamma + \left(\frac{2(\nu_M \cdot \nu_X)^{3/2}}{\nu} \right) m^2 \cdot C_{MX}^\gamma \quad (2.1)$$

where M and X are the cation and the anion, respectively. ν_M , ν_X , Z_M and Z_X are the ion number, the charge number of the cation and anion in each molecule, respectively, $\nu = \nu_M + \nu_X$. The extended form of the Debye-Hückel term f^γ and the form for the ion strength dependence of B_{MX}^γ are defined in Eqs. (2.2) and (2.3) respectively. C_{MX}^γ is related to C_{MX}^Φ .

$$f^\gamma = -A^\Phi \left[\frac{\sqrt{I_m}}{1 + b_p \sqrt{I_m}} + \frac{2 \ln(1 + b_p \sqrt{I_m})}{b_p} \right] \quad (2.2)$$

$$B_{MX}^\gamma = 2\beta_{MX}^{(0)} + \beta_{MX}^{(1)} \cdot g(\alpha_1 \cdot \sqrt{I_m}) + \beta_{MX}^{(2)} \cdot g(\alpha_2 \cdot \sqrt{I_m}) \quad (2.3)$$

$$C_{MX}^\gamma = 3C_{MX}^\Phi / 2 \quad (2.4)$$

I_m is the ionic strength of solution, and $I_m = (\sum_i Z_i^2 m_i) / 2$. b_p is an universal parameter with the value $1.2 (\text{mol} \cdot \text{kg}^{-1})^{-1/2}$. A^Φ is the Debye-Hückel coefficient for osmotic function, which has the value $0.3920 (\text{mol} \cdot \text{kg}^{-1})^{-1/2}$ at 25 °C.

In Eq. (2.3), for other than 2-2 salts (1-1-, 2-1-, 1-2-, 3-1-, 4-1-type salts) only the first two terms are considered with the value $\alpha_1 = 2.0 (\text{mol} \cdot \text{kg}^{-1})^{-1/2}$. Three terms are taken into account for all 2-2 salts at 25 °C with the values $\alpha_1 = 1.4 (\text{mol} \cdot \text{kg}^{-1})^{-1/2}$ and $\alpha_2 = 12.0 (\text{mol}$

$\text{kg}^{-1})^{-1/2}$. $\beta_{MX}^{(0)}$ and $\beta_{MX}^{(1)}$ represent short-range interactions. $\beta_{MX}^{(2)}$ is negative and is related to the association equilibrium constant. C_{MX}^Φ relates to short-range interactions of three ions.

The function of $g(x)$ is expressed as:

$$g(x) = 2 \left[1 - (1 + x - \frac{1}{2}x^2)e^{-x} \right] / x^2 \quad (2.5)$$

2.2.2 Activity coefficient for mixed electrolytes

In theory of mixed electrolytes, sums of neutral electrolyte composed by positive and negative ions are over the various cations and over the anions (Pitzer 1991):

$$\begin{aligned} \ln \gamma_M = & Z_M^2 F + \sum_{i_A=1}^{N_A} m_A (2B_{MA} + ZC_{MA}) + \sum_{i_C=1}^{N_C} m_C (2\Phi_{MC} + \sum_{i_A=1}^{N_A} m_A \Psi_{MCA}) + \\ & \sum_{i_A=1}^{N_A-1} \sum_{j_A=i_A+1}^{N_A} m_A m_{A'} \Psi_{AA'M} + |Z_M| \left[\sum_{i_C=1}^{N_C} \sum_{i_A=1}^{N_A} m_C m_A C_{CA} + \sum_{i_N=1}^{N_N} m_N (2\lambda_{NM}) \right] \end{aligned} \quad (2.6)$$

$$\begin{aligned} \ln \gamma_X = & Z_X^2 F + \sum_{i_C=1}^{N_C} m_C (2B_{CX} + ZC_{CX}) + \sum_{i_A=1}^{N_A} m_A (2\Phi_{XA} + \sum_{i_C=1}^{N_C} m_C \Psi_{XAC}) + \\ & \sum_{i_C=1}^{N_C-1} \sum_{j_C=i_C+1}^{N_C} m_C m_{C'} \Psi_{CC'X} + |Z_X| \left[\sum_{i_C=1}^{N_C} \sum_{i_A=1}^{N_A} m_C m_A C_{CA} + \sum_{i_N=1}^{N_N} m_N (2\lambda_{NX}) \right] \end{aligned} \quad (2.7)$$

$$\ln \gamma_N = \sum_{i_C=1}^{N_C} m_C (2\lambda_{AC}) + \sum_{i_A=1}^{N_A} m_A (2\lambda_{NA}) \quad (2.8)$$

In Eqs. (2.6) to (2.8), C and C' are cations and A and A' are anions. m_C is the molality of cation C and Z_C the charge number. N_C is the species number of the cations. Anion A and the neutral molecule have similar definition. M, X and N stand for cation, anion and neutral molecule, respectively.

$$\begin{aligned} F = & -A^\Phi \left[\sqrt{I_m} / (1 + 1.2\sqrt{I_m}) + 2 \ln(1 + 1.2\sqrt{I_m}) / 1.2 \right] + \sum_{i_C=1}^{N_C} \sum_{i_A=1}^{N_A} m_C m_A B_{CA}' + \\ & \sum_{i_C=1}^{N_C-1} \sum_{i_C'=i_C+1}^{N_C} m_C m_{C'} \Phi_{CC'}' + \sum_{i_A=1}^{N_A-1} \sum_{i_A'=i_A+1}^{N_A} m_A m_{A'} \Phi_{AA'}' \end{aligned} \quad (2.9)$$

$$C_{MX} = C_{MX}^\Phi / (2|Z_M Z_X|^{1/2}) \quad (2.10)$$

$$Z = \sum_i |Z_i| m_i \quad (2.11)$$

$$B_{CA} = \beta_{CA}^0 + \beta_{CA}^1 g(\alpha_1 \sqrt{I_m}) + \beta_{CA}^2 g(\alpha_2 \sqrt{I_m}) \quad (2.12)$$

$$B'_{CA} = [\beta_{CA}^1 g'(\alpha_1 \sqrt{I_m}) + \beta_{CA}^2 g'(\alpha_2 \sqrt{I_m})] / I_m \quad (2.13)$$

$$g'(x) = -2[1 - (1 + x + x^2/2) \exp(-x)] / x^2 \quad (2.14)$$

$$\Phi_{ij}^{\Phi} = \theta_{ij} + {}^E\theta_{ij} + I_m {}^E\theta'_{ij} \quad (2.15)$$

$$\Phi_{ij} = \theta_{ij} + {}^E\theta_{ij} \quad (2.16)$$

$$\Phi'_{ij} = {}^E\theta'_{ij} \quad (2.17)$$

$${}^E\theta_{ij} = (Z_i Z_j / 4 I_m) [J(x_{ij}) - J(x_{ii})/2 - J(x_{jj})/2] \quad (2.18)$$

$${}^E\theta'_{ij} = -({}^E\theta_{ij} / I_m) + (Z_i Z_j / 8 I_m^2) [x_{ij} J'(x_{ij}) - x_{ii} J'(x_{ii})/2 - x_{jj} J'(x_{jj})/2] \quad (2.19)$$

$$x_{ij} = 6 Z_i Z_j A^{\Phi} \sqrt{I_m} \quad (2.20)$$

$$J(x) = x [4 + C_1 x^{-C_2} \exp(-C_3 x^{C_4})]^{-1} \quad (2.21)$$

$$J'(x) = [4 + C_1 x^{-C_2} \exp(-C_3 x^{C_4})]^{-1} + [4 + C_1 x^{-C_2} \exp(-C_3 x^{C_4})]^{-2} [C_1 x \exp(-C_3 x^{C_4}) (C_2 x^{-C_2-1} + C_3 C_4 x^{C_4-1} x^{-C_2})] \quad (2.22)$$

Ψ is the interactions of three ions of different sign, which could be two cations and one anion, or two anions and one cation. B is the coefficient in the second dimension, which is related to ion strength. B' is the ion strength differential of B. $\beta_{CA}^{(0)}$, $\beta_{CA}^{(1)}$, $\beta_{CA}^{(2)}$ are characteristic parameters of electrolyte CA. $\beta^{(2)}$ is very important for 2-2 type or higher valence type electrolytes because electrolytes with high valence have a strong tendency of static association, whereas $\beta^{(2)}$ can be neglected for other valence types. For electrolytes with at least one monovalent ion, $\alpha_1 = 2.0$ (mol kg⁻¹)^{-1/2} and $\alpha_2 = 0$ can be used. For 2-2 electrolytes at 25 °C, $\alpha_1 = 1.4$ (mol kg⁻¹)^{-1/2}, $\alpha_2 = 12$ (mol kg⁻¹)^{-1/2}. Generally, it is supposed that α_1 and α_2 do not change by temperature. Φ accounts for interactions between ions of like charge (two cations or two anions), which arise only for mixed solutions. ${}^E\theta_{ij}$ and ${}^E\theta'_{ij}$ account for these electrostatic unsymmetrical mixing effects and they depend only on the charges of i and j and the total ion strength. When the charge quantity of i and j are equal, ${}^E\theta_{ij}$ and ${}^E\theta'_{ij}$ are zero. $J(x)$ is the group integration for short-range interaction potential energy. $J'(x)$ is the first order derivative of $J(x)$. $J(x)$ and $J'(x)$ only depend on ion strength and ion charge number. In Eqs. (2.21) and (2.22), $C_1 = 4.581$, $C_2 = 0.7237$, $C_3 = 0.012$, $C_4 = 0.528$ (Niu et al. 2001).

2.3 Solubility prediction of potassium chloride in a $\text{MgCl}_2\text{-KCl-H}_2\text{O}$ system

Solubility of KCl in an $\text{MgCl}_2\text{-KCl-H}_2\text{O}$ system was predicted successfully with a Pitzer theoretical model at 25 °C in this study (Han et al. 2009). The prediction is divided into three steps. The first step is to calculate the average activity coefficient of KCl with different molalities in pure potassium chloride solution by Eqs. (2.1) to (2.5). The second step is calculation of the solubility product of KCl. Based on the solubility of KCl in the ternary system from literature, $m_{(\text{KCl})}$ is known. The solubility product (Myerson 2002) can be calculated by Eq. (2.23):

$$K_{\text{sp}(\text{KCl})} = \gamma_{\pm}^2 m_{\pm}^2 \quad (2.23)$$

$\gamma(\text{KCl})$ is calculated from the first step. Thus, the solubility product of KCl is taken from pure KCl solubility data, i.e. a binary solution. In an $\text{MgCl}_2\text{-KCl-H}_2\text{O}$ ternary system, activity coefficients of K^+ and Cl^- can be calculated from Eq. (2.6) to (2.22). Then $\gamma_{\pm(\text{KCl})}$ is known in the third step. The parameter values used in the calculations are summarized in Table 2.1. Because the solubility product only depends on temperature, $K_{\text{sp}(\text{KCl})}$ is constant in pure KCl and ternary solutions. Thus, the solubility of KCl in the ternary system can be backward predicted by Pitzer model by iterating. Comparison of the predicted and reference data is shown in Figure 2.1 (Han et al. 2009).

Table 2.1 Pitzer parameters used in the calculation (Pitzer 1991, Niu et al. 2001).

$\beta_{\text{KCl}}^{(0)}$	$\beta_{\text{KCl}}^{(1)}$	C_{KCl}^{Φ}	$\beta_{\text{MgCl}_2}^{(0)}$	$\beta_{\text{MgCl}_2}^{(1)}$	$C_{\text{MgCl}_2}^{\Phi}$	$\theta_{\text{K,Mg}}$	$\psi_{\text{K,Mg,Cl}}$
0.04835	0.2122	-0.00084	0.35235	1.6815	0.00519	0	-0.022

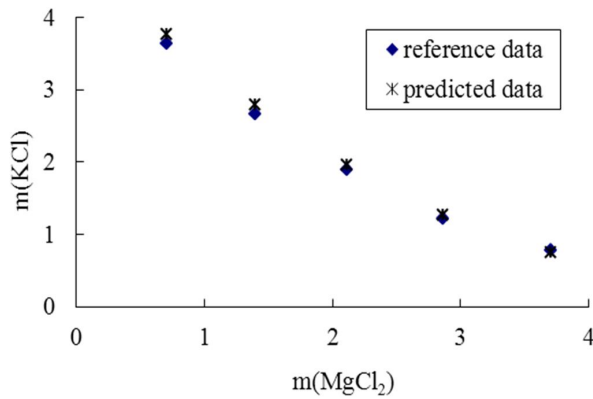


Figure 2.1 Predicted results compared with literature data (Han et al. 2009).

2.4 Solubility of potassium dihydrogen phosphate in aqueous solutions containing non-electrolyte organic compounds (Publication II)

2.4.1 Experimental section

Solubility of potassium dihydrogen phosphate (KH_2PO_4 , KDP) in different mixtures of water and three non-electrolytes, acetone, ethyl acetate and thiourea, were measured by gravity analysis method in the temperature range of (298.15 to 313.15) K. The molality of acetone in the solvent was in the range of (0.441 to 5.739) $\text{mol}\cdot\text{kg}^{-1}$. For ethyl acetate, two molalities, 0.291 and 0.597 $\text{mol}\cdot\text{kg}^{-1}$, were used. For thiourea, molalities of 0.200 to 1.50 $\text{mol}\cdot\text{kg}^{-1}$ were used. The experimental method is described in detail in Publication II.

2.4.2 Results and discussion

Solubility of KH_2PO_4 in water

In order to check if the method used in solubility measurement is reliable and accurate, solubility experiments of KH_2PO_4 in water were checked at four temperatures: 298.15, 303.15, 308.15, and 313.15 K. Comparison of the results of this work and reference data is shown in Figure 2.2.

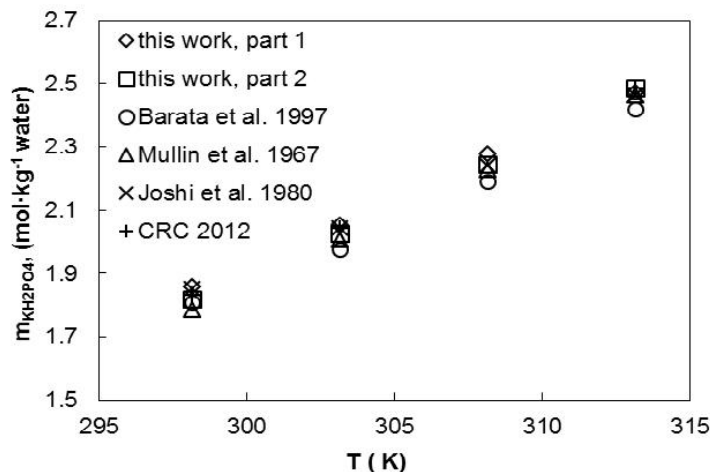


Figure 2.2 Comparison of experimental and reference solubility data of KH_2PO_4 in water at (298.15, 303.15, 308.15, and 313.15) K. Part 1 and Part 2 mean that the data were obtained in Tianjin and Lappeenranta respectively.

It can be seen from Figure 2.2 that the experimental data agreed well with the reference data. The average relative deviation is smaller than 3.2 %. Therefore, it can be concluded that the method used in this work can reliably obtain accurate solubility data.

Solubility of KH_2PO_4 in mixed solvents

For the same composition of solvent, solubility of KH_2PO_4 increased with increase in temperature in the three mixtures studied: (water + acetone), (water + ethyl acetate) and (water + thiourea). The solubility of KDP decreased with increasing concentration of non-electrolytes at constant temperature. The results predicted by the Pitzer thermal model agreed consistently well with the experimental data. The critical Pitzer parameter concerning interactions for ions and non-electrolyte molecules, λ , can explain the effect of non-electrolyte on the solubility of KH_2PO_4 .

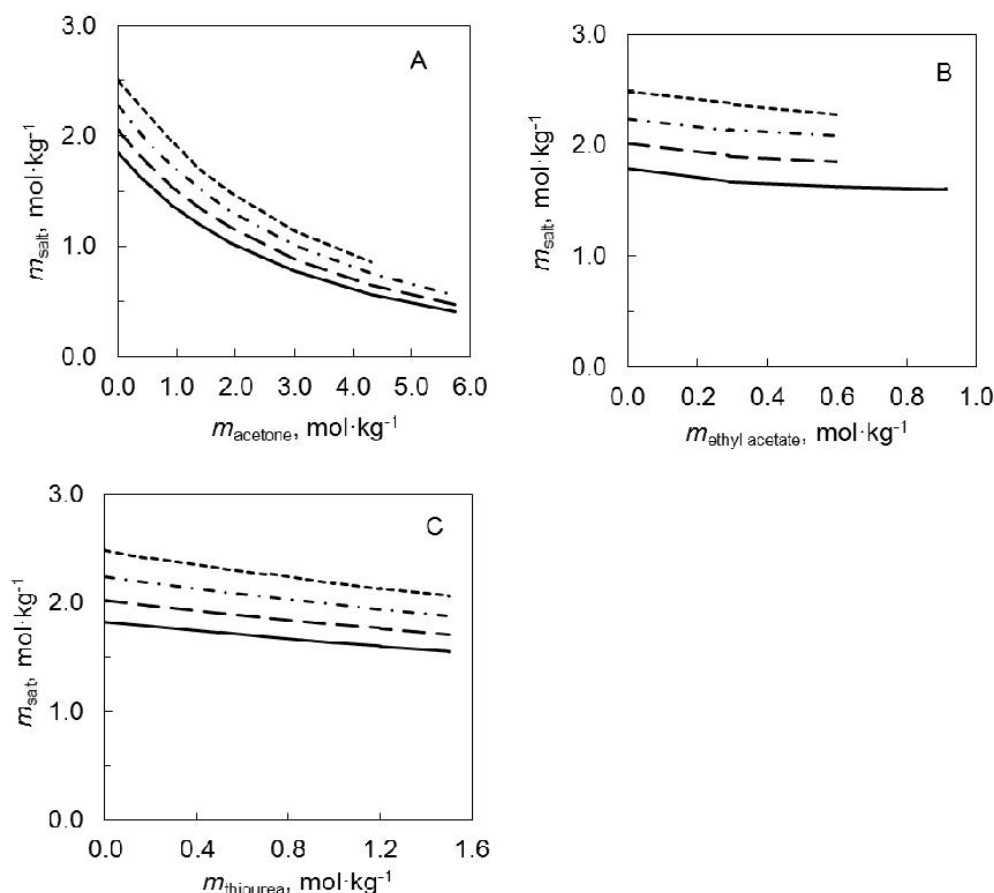


Figure 2.3 Solubility of KH_2PO_4 , expressed as the molality of the salt (m_{salt}), as a function of the nonelectrolyte (m) in mixtures of water with acetone (A), ethyl acetate (B), and thiourea (C) at the following temperatures: —, $T = 298.15$ K; — —, $T = 303.15$ K; - · -, $T = 308.15$ K; - - -, $T = 313.15$ K.

Figure 2.3 shows the solubility of KH_2PO_4 affected by non-electrolyte solvents. The results show that acetone has a big effect on the solubility of KH_2PO_4 , whereas ethyl acetate and thiourea do not influence the solubility very much. In addition to the solubility data obtained from the present study, the solubility of KH_2PO_4 in three mixtures of water

with urea, ethanol and 1-propanol at 303.15 K has been reported in literature (Partanen et al. 2003, Barata et al. 1997). Therefore, in order to directly observe the effect of different solvents on the solubility of KH_2PO_4 , comparable results are shown in Figure 2.4. It can be seen that the solubility is most affected by alcohol (ethanol, 1-propanol, acetone), with smaller effects found for thiourea and ethyl acetate. Urea has the least impact. The results provide valuable information for the selection of solvent in crystallization processes. To get the desired crystallized product, a suitable solvent and its concentration can be correctly chosen based on the prediction trend, thus saving time and costs and promoting work efficiency.

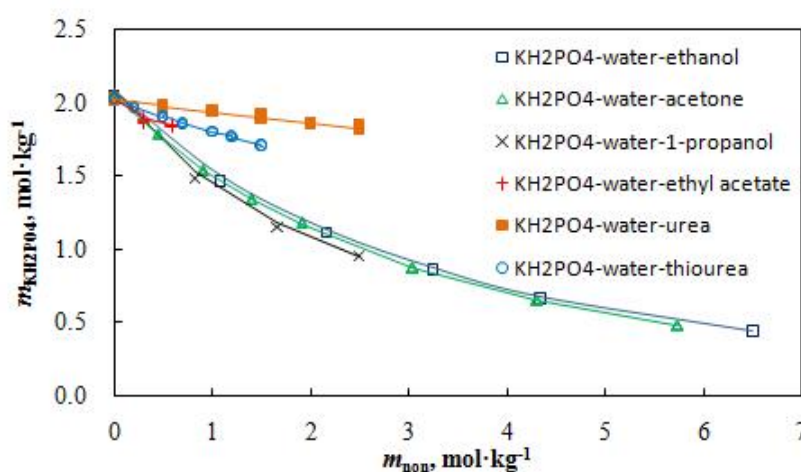


Figure 2.4 Comparison of measured and calculated solubilities against non-electronic concentrations at 303.15 K. Symbols stand for experiments and curves for predictions.

2.5 Summary

In this chapter, application of the Pitzer thermodynamic model to prediction of the solubility of KCl in MgCl_2 -KCl- H_2O ternary system was theoretically studied. It was noted that the activity coefficient and solubility of KCl at 25 °C can be predicted through an iteration method with the solubility product and the Pitzer model. New solubility data for KH_2PO_4 in aqueous solutions of acetone, ethyl acetate and thiourea in the temperature range of (298.15-313.15) K were obtained experimentally. It was further noted that the established function of parameter λ and temperature reflects well the influence of non-electrolyte on the solubility of KH_2PO_4 . The optimal condition of this model is that the molality should be smaller than 6 $\text{mol}\cdot\text{kg}^{-1}$. This is probably the limitation of the model since the impact of non-electrolyte can be easily considered by the relationship of λ and T . The present work demonstrated that the Pitzer model can be effectively applied to solubility prediction from aqueous KDP solutions containing organic compounds.

3. Reactive crystallization of magnesium carbonate

3.1 Magnesium carbonate precipitates

The present work focuses on carbonate precipitation with CO₂ gas and the selected model compound was magnesium carbonate. Influence of variables such as temperature, gas flow rate and stirring rate on pH of the solution, particle size distribution and crystal shape of precipitate in the heterogeneous system was investigated and discussed. From offline and inline measuring methods obtained kinetic data on various simultaneously occurring phenomena give insight into the mechanism of the studied gas-liquid reactive crystallization which is a part of precipitation.

3.1.1 Formation of magnesium carbonates

Magnesium carbonate compounds can consist of different ratios of magnesium hydroxide, magnesium carbonate and water depending on pH and temperature. There are many hydrous forms, such as barringtonite (MgCO₃·2H₂O), nesquehonite (MgCO₃·3H₂O), lansfordite (MgCO₃·5H₂O), artinite (Mg₂CO₃(OH)₂·3H₂O), hydromagnesite (Mg₅(CO₃)₄(OH)₂·4H₂O) and dypingite (Mg₅(CO₃)₄(OH)₂·5H₂O). The anhydrous form, magnesite (MgCO₃), is usually hard to synthesize. It is the most stable Mg-carbonate compound at elevated temperature. For example, Hänchen et al. (2008) reported that magnesite formed at 120 °C and CO₂ pressure of 100 bar. At ambient temperature, it is impossible to precipitate magnesite.

In general, hydrated forms of magnesium carbonate are much easier to produce than the anhydrous form. This is attributed to the highly hydrated character of Mg²⁺ in solution. The initial appearance of thermodynamically unstable phases is a common phenomenon and often related to Ostwald's rule of stages (Mullin 2001). For instance, nesquehonite formed initially could be gently replaced by the less hydrated compound hydromagnesite. Water molecules being dipoles have strong electrostatic interaction with all ions. The electrostatic force can form a barrier around the Mg cations and the cations easily incorporate into the carbonate structure (Hänchen et al. 2008). Molecular dynamics simulations indicate that Mg²⁺ is a little smaller than Ca²⁺ and thus result in higher charge density, but the lifetime of water molecules surrounding Mg²⁺ is in the order of hundreds of picoseconds, in contrast to only a few picoseconds for Ca²⁺, K⁺, or Na⁺ (Jiao et al. 2006). Therefore, the extremely high hydrophilic nature of Mg²⁺ restricts the formation of anhydrous carbonates through magnesium in anti-solvent process.

3.1.2 Production of magnesium carbonate by homogeneous liquid reaction

Dong et al. (2008, 2009) investigated the solubility and stability of nesquehonite in several single salt and two salt solutions in the temperature range of 15 to 35 °C. In single salt solutions (NaCl, KCl, MgCl₂, and NH₄Cl), the solubility of nesquehonite decreased with increasing temperature, whereas it rose in mixed solutions (NaCl+MgCl₂, NH₄Cl+MgCl₂, LiCl, and LiCl+ MgCl₂). With the exception of NaCl solution, the solubility

increased with the addition of other single salts. The solubility increased with increasing concentration of magnesium due to the formation of MgHCO_3^+ . The pH decreased with increasing concentration of ammonium chloride, which resulted in an increase in the solubility because of the increase of H^+ .

Since abundant valuable chemicals in MgCl_2 brine, fabrication of these chemicals from brine has been attracted interest due to its low-cost, high-purity and large-scale compared with traditional method. Because of its good filtration characteristics, nesquehonite has been studied by many researchers from the reaction of MgCl_2 and $\text{NaCO}_3 / (\text{NH}_4)_2\text{CO}_3$ (Wang et al. 2008, Cheng et al. 2009, 2010). Nucleation kinetics and the effect of parameters such as temperature, initial concentration and stirring speed on crystal properties (morphology and particle size) have been investigated. Crystals of nesquehonite are generally needle-like. Fine petaloid microspheres of basic magnesium carbonate ($x\text{MgCO}_3 \cdot y\text{Mg}(\text{OH})_2 \cdot z\text{H}_2\text{O}$) have been obtained through ultrasonic irradiation by soda ash method from the reaction of $\text{MgSO}_4 \cdot 7\text{H}_2\text{O}$ with Na_2CO_3 . (Ohkubo et al. 2007).

3.1.3 Production of magnesium carbonate by heterogeneous gas-liquid reaction

Chemical trapping is a potential method for capture and storage of CO_2 . Precipitation was carried out in a $\text{H}_2\text{O}-\text{CO}_2-\text{Na}_2\text{CO}_3-\text{MgCl}_2$ system at temperatures between $25\text{ }^\circ\text{C}$ and $120\text{ }^\circ\text{C}$ and at a partial pressure of CO_2 between 1 and 100 bar. The supersaturation level affects the forms of magnesium carbonate (Hänchen et al. 2008). Microtubes of basic magnesium carbonate ($x\text{MgCO}_3 \cdot y\text{Mg}(\text{OH})_2 \cdot z\text{H}_2\text{O}$) with a surface “house of cards” structure have been synthesized from the reaction between magnesium hydroxide and carbon dioxide by adding NaOH solution. The product was formed through needlelike particles of magnesium carbonate trihydrate (Mitsuhashi et al. 2005). Ferrini et al. (2009) reported a novel method to synthesize nesquehonite via the reaction of magnesium chloride with CO_2 at $20 \pm 2\text{ }^\circ\text{C}$. Ammonia solution was used to adjust pH to around 7.8-8.2 to obtain nesquehonite. Teir et al. (2007, 2009) investigated a method to produce magnesium carbonate from serpentinite (abundant magnesium) for permanent storage of CO_2 . Serpentinite was firstly dissolved in acid (HCl/HNO_3) at high temperature. Then the magnesium salt precipitated is obtained after evaporation of excess solvent. Magnesium carbonate can be precipitated into the solution by bubbling CO_2 , which is mixed by magnesium salt and water under alkalinity conditions. Suitable pH for precipitation of magnesium carbonates is 9.

3.2 Factors impacting the particle size distribution of magnesium carbonate

3.2.1 Experimental part

A 3 L crystallizer equipped with a jacket was used for semi-batch crystallization. A specifically defined amount of $\text{Mg}(\text{OH})_2$ (purity $\geq 99.6\%$) mixed with deionized water was put into the crystallizer. Gaseous CO_2 (purity $\geq 99.7\%$) was fed from the bottom of the

crystallizer through a sparger into the prepared $\text{Mg}(\text{OH})_2$ suspension when the temperature achieved the target temperature. Slurry samples were taken during the process. Solids were filtered and dried at room temperature for later analysis. Beckman Coulter LS13320 laser particle size analyzer and X-ray diffraction were used for the characterization of the obtained crystals. The experimental procedure and obtained crystal size distributions are introduced in further detail in the publications (Han et al. 2012, Han et al. 2014). Figures A1 to A6 in Appendix A show the main results obtained by Han et al. (2014). Selected impact factors are listed in Table 3.1.

Table 3.1 Selected experimental impact factors.

Factors	Values
Temperature	25 °C, 40 °C, 62 °C
Size of gas sparger	40 μm , 60 μm
Initial concentration of $\text{Mg}(\text{OH})_2$ slurry	2.0 %, 2.9 %, 3.8 %
Size of $\text{Mg}(\text{OH})_2$	Grinding and without grinding

3.2.2 Results and discussion

Temperature

It was found that magnesium carbonate trihydrate was produced at all three temperatures. This finding differs from results published in literature (Shao et al. 2009, Botha et al. 2001), which reported that magnesium carbonate trihydrate could transfer to hydromagnesite during 55-65 °C. The reason might be that reactive conditions in the gas-liquid and liquid-liquid reaction are different. The slurry pH decreased faster at higher temperature, which is shown in Fig. 3.1. Fig. 3.2 shows that a large amount of magnesium carbonate was already formed at 10 min at 62 °C, whereas only a small amount formed at 40 °C and almost no magnesium carbonate was produced at 25 °C. Thus, the reaction rate increases with increasing temperature. Moreover, the $\text{Mg}(\text{OH})_2$ slurry reaction with CO_2 is an exothermic process, and temperature increases at the beginning of the reaction which can be seen in temperature data shown in Fig 3.1. The results also demonstrated that the greater the temperature increase, the faster the reaction is. Thus, the particle size of magnesium carbonate precipitate increases with temperature (Fig. 2 in Han et al. 2014). However, at 62 °C there is a dual peak of particle size distribution, because primary crystals agglomerated due to the formation of a great amount of magnesium carbonate crystal nuclei during a short time.

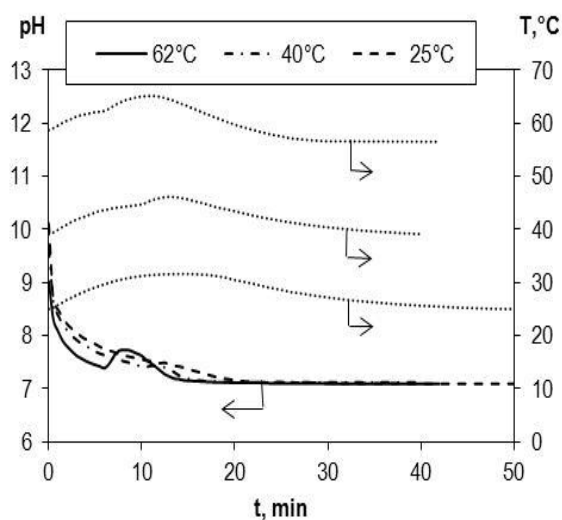


Fig. 3.1 Time dependence of pH and temperature at 25, 40, and 62 $^{\circ}\text{C}$. Experimental conditions: gas flow rate 9 L/min, pore size of sparger 60 μm , initial slurry concentration 3.8 %. Temperature profiles expressed as ‘.....’.

Pore size of gas sparger

With constant CO_2 flow, the pH is reduced faster with the sparger of bigger pore size (Fig. 3.3). From XRD diagrams (comparison of Fig. 3.2c and Fig. 3.4), it can be seen that the solid mainly was $\text{Mg}(\text{OH})_2$ with a sparger of 40 μm at 15 min, whereas a certain amount of magnesium carbonate already existed in the system with a sparger of 60 μm , which indicates that reaction rate is faster with the sparger of larger pore size. As a consequence, there is more time for crystal growth and thus larger particles are produced with a bigger pore size gas sparger (Fig. 3 in Han et al. 2014).

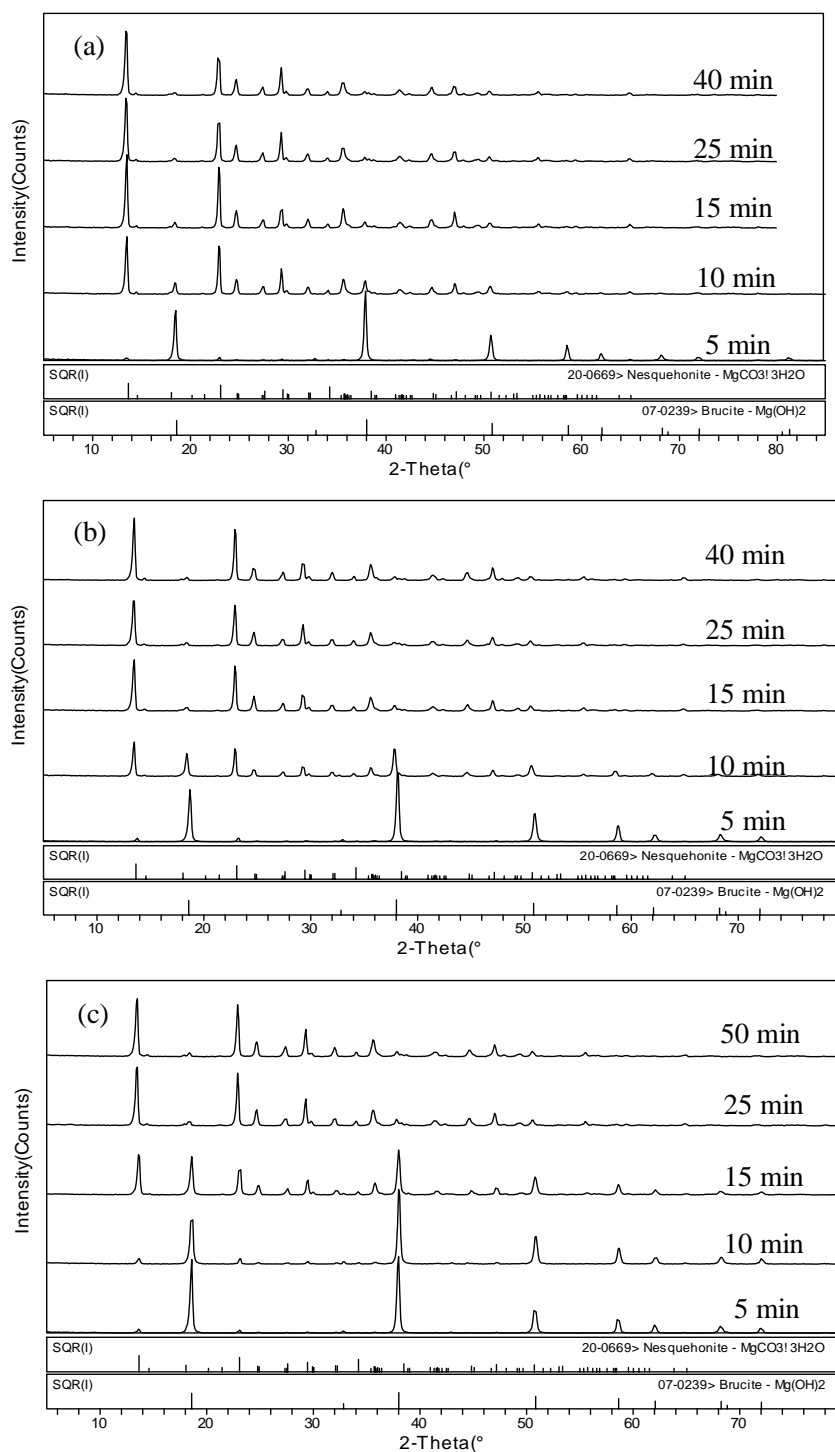


Fig. 3.2 XRD pattern for solid samples taken at different time at 62°C (a), 40°C (b), 25°C (c) together with reference data.

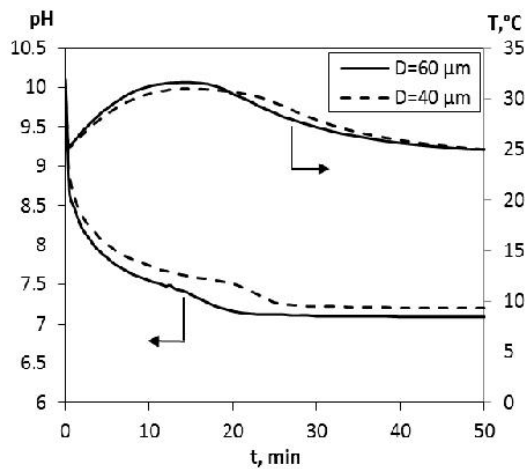


Fig. 3.3 Time dependence of pH and temperature for two pore sizes of sparger. Experimental conditions: gas flow rate 9 L/min, temperature 25°C, initial slurry concentration 3.8 %.

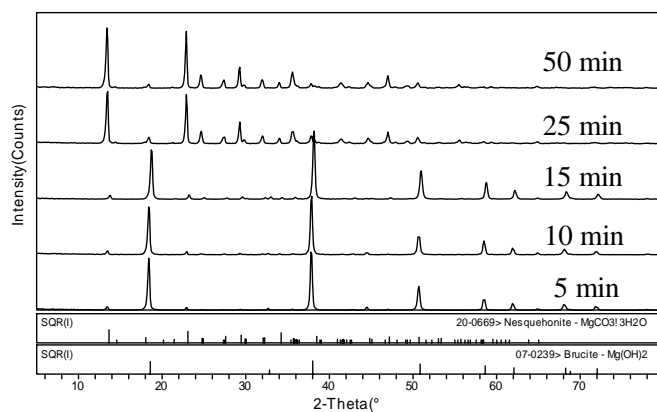


Fig. 3.4 XRD pattern for solid samples taken at different times with a sparger of pore size 40 μm .

Initial slurry concentration of magnesium hydroxide

The pH of the system decreased with decreasing initial concentration of $\text{Mg}(\text{OH})_2$ (Fig. 4 in Han et al. 2014). With a CO_2 flow rate of 9 L/min, there was no precipitate when initial concentration was 2.0 %. The lack of precipitate may be because all $\text{Mg}(\text{OH})_2$ was reacted to aqueous $\text{Mg}(\text{HCO}_3)_2$ due to the high flow rate of CO_2 . This explanation is supported by the work of Mitsuhashi et al. (2005), who used an aqueous solution of $\text{Mg}(\text{HCO}_3)_2$ produced by $\text{Mg}(\text{OH})_2$ and CO_2 to control the crystal shapes of magnesium carbonates. In order to establish if CO_2 flow (9 L/min) is too high for precipitation, a lower flow rate (1 L/min) was tested at other constant experimental conditions. For this lower flow rate, a small amount of magnesium carbonate was precipitated. The results

indicate that pH is really important throughout the whole reactive crystallization and the reactive crystallization can be controlled by adjusting initial $\text{Mg}(\text{OH})_2$ slurry concentration and CO_2 flow rate.

Smaller crystals were obtained with initial concentration of $\text{Mg}(\text{OH})_2$ of 3.8 % (Fig. 5 in Han et al. 2014). At the beginning of the reaction, magnesium concentrations were the same for different solid contained slurries of $\text{Mg}(\text{OH})_2$. With gaseous CO_2 introduced into the system, the dissolution rate increased due to the pH reduction. There were many more particles when the $\text{Mg}(\text{OH})_2$ suspension density was higher. Therefore, the interfacial area was relatively higher between the solid and liquid phases, thus resulting in the higher dissolution rate. Consequently, the supersaturation of magnesium carbonate was increased, which increased the nucleation rate. The obtained particle size was then smaller with higher slurry concentration.

Crystal size of magnesium hydroxide

The median size of raw material and grinding magnesium hydroxide were $6.6\ \mu\text{m}$ and $2.9\ \mu\text{m}$, respectively (Fig. 6 in Han et al. 2014). At CO_2 flow rate of 5 L/min, pH profiles and particle size distribution (shown in Fig. 3.5) were almost the same for the two different initial $\text{Mg}(\text{OH})_2$ particle sizes. However, when the CO_2 flow rate was increased to 9 L/min, the reduction in initial $\text{Mg}(\text{OH})_2$ particle size accelerated the decrease of pH. Thus larger particles of magnesium carbonate were formed (Fig. 7 in Han et al. 2014).

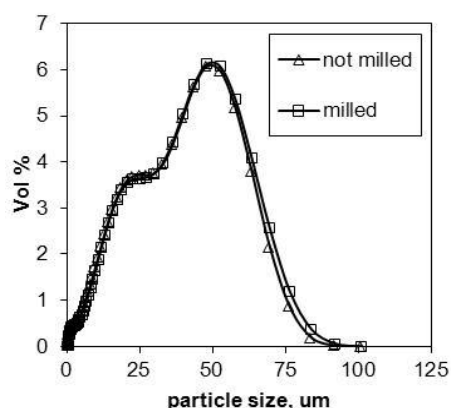


Fig. 3.5 Particle size distribution using different size of $\text{Mg}(\text{OH})_2$. Experimental conditions: gas flow rate 5 L/min, temperature 25°C , pore size of sparger $40\ \mu\text{m}$, initial slurry concentration 3.8 %.

The dissolution surface area increased because of the decrease in particle size of the reactant. This led to increased dissolution rate. However, the crystallization process is mainly controlled by the absorption of CO_2 . Therefore, a low flow rate of CO_2 does not affect particle size distribution significantly, whereas a high flow rate of CO_2 can enhance the gas-liquid mass transfer. The supersaturation is increased, which promotes the crystal growth, obtaining larger crystals.

3.3 Precipitation kinetics of magnesium carbonate

3.3.1 Experimental section

Experimental method

Based on investigation of impact factors on magnesium carbonate discussed in Chapter 3.2, temperature of 25 °C, pore size of sparger of 40 μm and initial magnesium hydroxide concentration of 3.8 % were kept constant in the experiments. Two other main factors, gas flow rate and stirring rate, were chosen to study precipitation kinetics. A number of experiments of oxygen absorption in water were also carried out to investigate mass transfer of gaseous CO_2 absorption. Detailed description of the experimental materials and methods are introduced in Publications IV and V.

Raman spectroscopy

The Raman spectra of reactant $\text{Mg}(\text{OH})_2$ and precipitant $\text{MgCO}_3 \cdot 3\text{H}_2\text{O}$ are shown in Fig. 3.6. Characteristic peaks of $\text{Mg}(\text{OH})_2$ and $\text{MgCO}_3 \cdot 3\text{H}_2\text{O}$ appeared at 278 cm^{-1} , 443 cm^{-1} , and 1100 cm^{-1} , respectively. The results show that Raman spectrometry can be used for identifying solid samples because there were no overlapped peaks between the spectra of the two compounds.

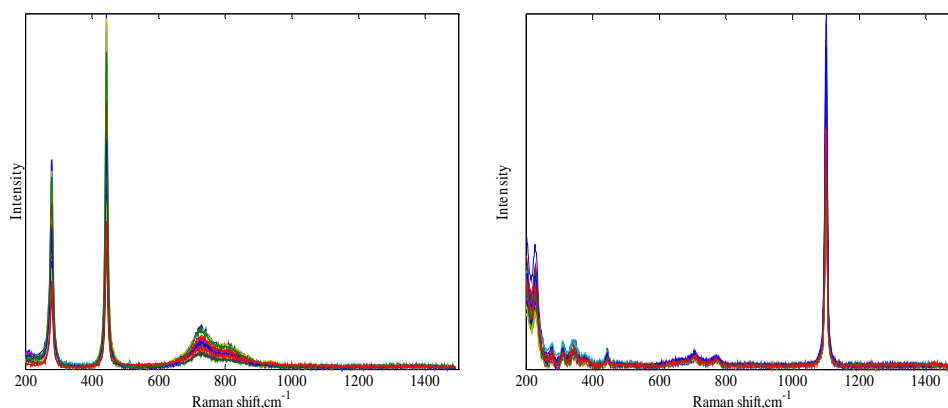


Fig. 3.6 Raman spectrum of magnesium hydroxide (left) and magnesium carbonate trihydrate (right).

Experiments for calibration of Raman spectra are described in Publication IV. A Bruker Raman spectrometer with OPUS software can be used to create calibration models based on different mathematical methods. The optimal model given for the present system is multiplicative scatter correction. The range of wavenumber is 195~1095 cm^{-1} , and the correlation coefficient is 98.19. The calibration results can be seen in Fig. 3.7.

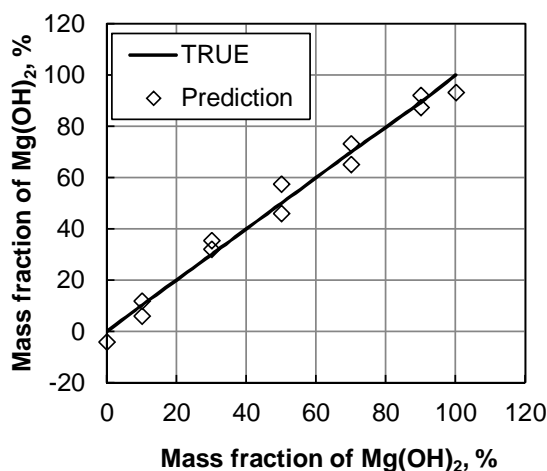


Fig. 3.7 Raman calibration model by multiplicative scattering correction.

Based on the investigation of Raman spectrometry by the author in Publication I and reports in the literature (One et al. 2004, Hatakka et al. 2010, Agarwal et al. 2010), use of a univariate calibration model (namely the ratio of peak height) is an easy and simple method to establish the Raman calibration model. The relationship of the composition of the mixtures and ratio of peak height is shown in Fig. 3.8. The expression of the model can be found in Publication IV.

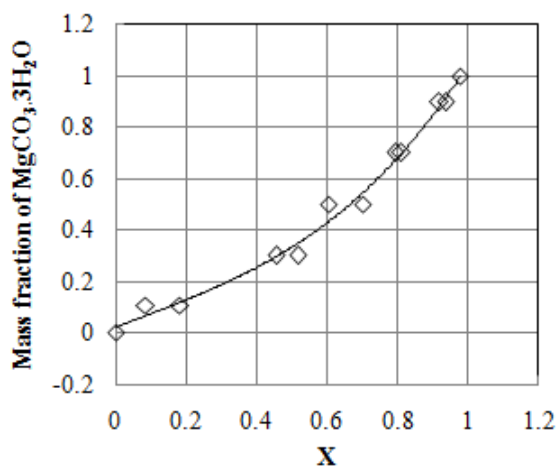


Fig. 3.8 Raman calibration model by univariate method, symbol and solid line stand for experimental data and fitting line respectively.

When comparing these two calibration methods, the univariate method with coefficient R^2 of 0.9905 is better than the method used by OPUS. On the one hand, the current study focused on an inorganic compound system. Therefore, the obtained spectrum is relatively simple compared with other complex system, such as various organic compound systems.

On the other hand, it may be so that in the present study only seven mixtures used for calibration were not enough to generate multivariate model. Or it might include other irrelevant information during fitting for this simple system by multivariate method. Therefore, it can be concluded that univariate peak height ratio method is much better than multivariate method. Patel et al. (2001) also reported that univariate method was more suitable for simple system than multivariate method in transformation of sulfathiazole crystalline forms.

Thermal analysis method (Publication V)

A simple mathematic model was established to determine the composition of solid mixtures. Detailed thermal analysis method was introduced in Publication V.

3.3.2 Effect of CO₂ flow rate (Publications IV and V)

At constant temperature and stirring speed, the increase of flow rate of CO₂ can promote the precipitation of magnesium carbonate. Moreover, the volumetric mass transfer coefficient (k_{La}) of oxygen was enhanced by increasing gas flow rate, which reflects the similar trend of predicted k_{La} for CO₂. The results are shown in Publication IV. The results obtained both from precipitation and mass transfer experiments indicate that absorption of CO₂ plays a key role in the semi-batch precipitation process of magnesium carbonate. Nucleation started earlier with higher flow rate and there were more time for crystal growth. Then the larger particles of magnesium carbonate were obtained.

3.3.3 Effect of stirring speed (Publications IV and V)

At constant temperature and flow rate of CO₂, stirring rate has an effect on dissolution of magnesium hydroxide. Generally, high mixing rate can accelerate the dissolution of the substance. However, dissolution of Mg(OH)₂ was not enhanced with the highest stirring rate used in the study, 750 rpm. It was found that a mixing rate of 650 rpm was the optimal speed in the studied magnesium carbonation process. From the onset of the absorption experiments (Publications IV), k_{La} was enhanced with increase in rotation speed at constant flow rate. The absorption rate of gaseous CO₂ increased. The studied carbonation system is a heterogeneous reaction. Hence, bubbles and particles have interactions with each other and mass transfer phenomena occur throughout the whole process. Factors such as bubble size, particle size and shape, and crystal aggregation have an impact on the particle size of the final precipitate product.

3.3.4 Characteristics of the crystallized product (Publication V)

Nesquehonite (MgCO₃·3H₂O) was produced from the slurry of magnesium hydroxide and CO₂ gas. The crystals of nesquehonite are mostly needle-like shaped particles and aggregated with each other. The XRD results show the high crystallinity of the obtained nesquehonite crystals. Some small flaky crystals on the needle shaped particles were found in the middle of the precipitation process.

3.4 Carbonation process monitored by in-line Raman spectroscopy

3.4.1 Experimental section

Materials and methods

An immersed Raman probe (Kaiser Optical system) was used to monitor the precipitation process of magnesium carbonate. The wavelength of the laser was 785 nm. The spectra were captured with an exposure time of 30 s with two accumulations. The interval time between two measurements was 65 s. The total duration was 60 min for each semi-batch process. Temperature of 25 °C, flow rate of 1 L/min and stirring rate of 650 rpm were used as experimental conditions. The experimental procedure is the same as used in Publications IV and V.

Raman Calibration

Ten aqueous solutions of NaHCO_3 with the concentration of 0.1, 0.2, 0.25, 0.31, 0.35, 0.4, 0.5, 0.61, 0.7 and 1 mol/L were used in calibration to determine the concentration of HCO_3^- from the Raman peak area. Fifteen aqueous solutions of Na_2CO_3 with the concentration of 0.1, 0.2, 0.25, 0.31, 0.35, 0.40, 0.45, 0.51, 0.55, 0.60, 0.65, 0.71, 0.8, 0.9 and 1 mol/L were used to generate the calibration model for CO_3^{2-} . The characteristic peaks used in calibration for HCO_3^- (Fig. 3.9) and CO_3^{2-} (Fig. 3.10) were at 1020 and 1066 cm^{-1} , respectively. These two calibration models are shown individually in Fig. 3.11 and Fig. 3.12. It can be seen that good calibration models can be produced by univariate method for the two ions considered.

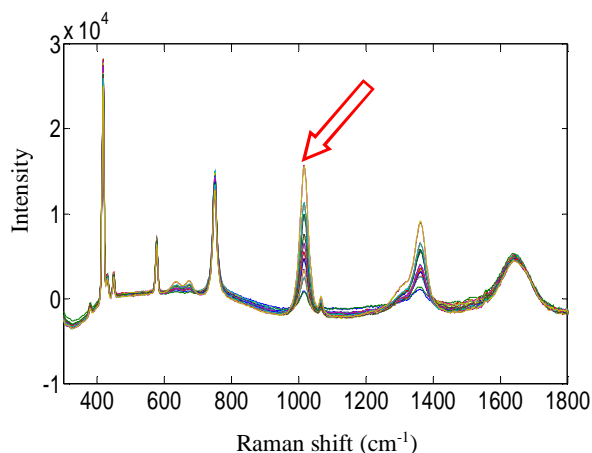


Fig. 3.9 Spectrum of NaHCO_3 solutions with different concentration.

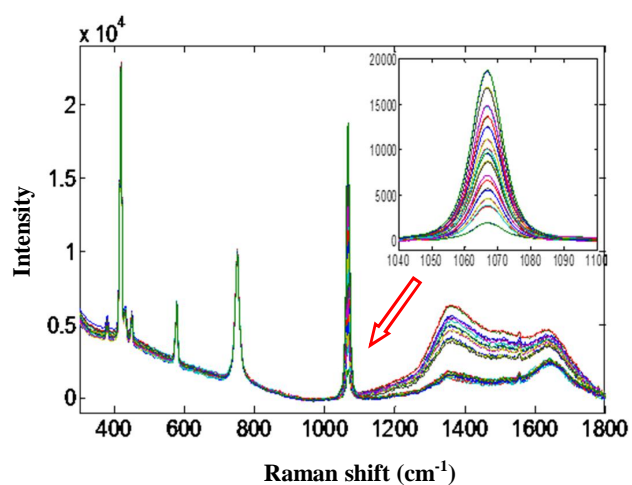


Fig. 3.10 Spectrum of Na_2CO_3 solutions with different concentration.

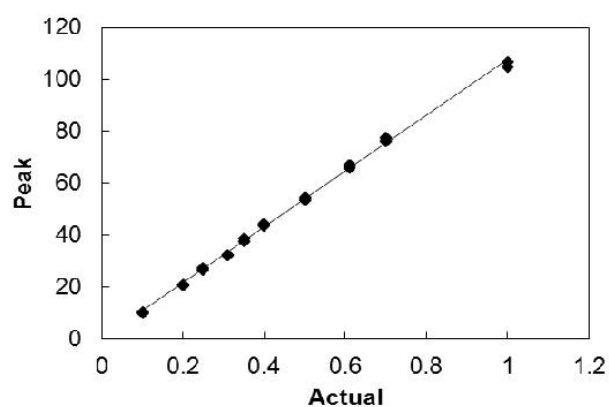


Fig. 3.11 Raman calibration model generated by univariate method for HCO_3^- .

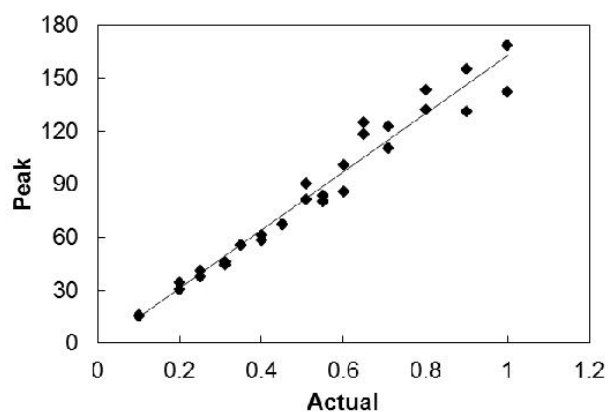


Fig. 3.12 Raman calibration model established by univariate method for CO_3^{2-} .

3.4.2 Results and discussion

With the addition of CO_2 flow, the formation of magnesium carbonate can be clearly seen from the characteristic peaks located at wavelength of 1100 cm^{-1} , as shown in Fig. 3.13. Ten samples were taken during precipitation and analyzed by TOC to determine the concentration of total carbon in the liquid phase.

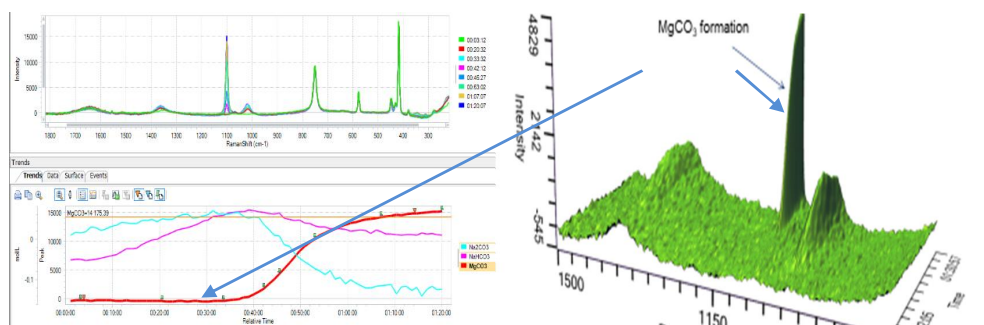


Fig. 3.13 Formation of magnesium carbonate from semi-batch precipitation.

Fig. 3.14 compares inline and offline results for carbon concentration. The predicted total carbon was calculated by the sum of HCO_3^- and CO_3^{2-} obtained from inline monitoring. It can be seen that the inline results agreed well with offline measurements. During the precipitation the concentration of CO_3^{2-} is very low and most of the carbon is the bicarbonate ion in the liquid. Titration with hydrochloride acid was used to determine the concentration of these two ions offline. However, the concentrations could not be determined due to the very great deviation. Raman inline monitoring gives more valuable information about individual compounds. The expected results of real-time information about the reactive crystallization process were successfully captured by the Raman immersion probe. However, the dissolution of $\text{Mg}(\text{OH})_2$ could not be monitored by the Raman probe used due to overlapping of the characteristic peak of $\text{Mg}(\text{OH})_2$ and the peak of the sapphire window of the Raman probe.

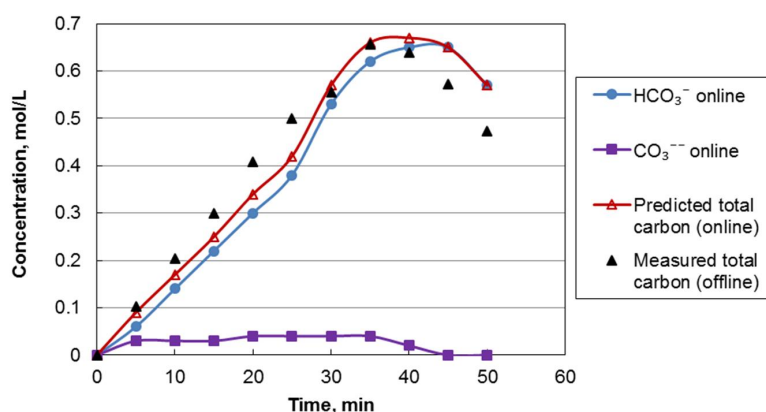


Fig. 3.14 Comparison of carbon concentration obtained by inline and offline measurements.

3.5 Summary

Magnesium carbonate trihydrate can be formed with proper operating conditions through the reactive crystallization of magnesium carbonate from the reaction of magnesium hydroxide and carbon dioxide at room temperature and atmospheric pressure. The favorable pH for the formation of nesquehonite is 7-7.6, which means that reactant Mg(OH)_2 is completely reacted.

The increase of temperature and pore size of gas sparger results in larger particles of magnesium carbonate, whereas smaller particles were precipitated with higher initial concentration of Mg(OH)_2 slurry. Particle size of Mg(OH)_2 has no effect on particle size distribution of magnesium carbonate with lower gas flow rate. However, this effect was significant as flow rate of CO_2 increased. It gives basic idea of how to control particle size distribution of magnesium carbonate in the heterogeneous system.

The effects of flow rate and stirring rate on the precipitation of magnesium carbonate were investigated in detail. The trends of consumption of magnesium hydroxide obtained with Raman spectrometry agreed quite well with the results obtained with the thermal analysis method. Therefore, the kinetics and mechanism of the magnesium carbonation process can be explained well from both the solid and liquid phases. As a result, stirring rate has an impact on dissolution rate of Mg(OH)_2 . Mass transfer of CO_2 absorption is one of the main factors in the current heterogeneous reaction system.

Tests of inline monitoring with an immersed Raman probe gave plenty of valuable data. The concentrations of HCO_3^- and CO_3^{2-} of filtrate samples, which are extremely difficult to measure offline by titration, with short time intervals, can be determined based on the developed Raman calibration models. Moreover, the formation of magnesium carbonate can be monitored from the Raman spectra.

In the future, more experiments are needed to find a way to quantify how much magnesium carbonate is formed during precipitation. Real-time information about the liquid and solid phases can be obtained and quantified from the Raman spectra simultaneously. Such information would be a significant improvement in understanding of the mechanisms and kinetics of the whole heterogeneous carbonation process. Inline measurements, i.e. real-time process monitoring, can be considered a more accurate method than offline analysis by sampling. In offline analysis from the stirred tank the chemical reactions and precipitations may continue in the taken samples, which can result in inaccurate kinetic data. Therefore, appropriate inline analysis methods are favorable. As a summary, it can be concluded that Raman analysis can yield accurate real-time data on the evolution of crystallization during a semi-batch precipitation process.

4. Mass transfer of absorption in the presence of suspended solid particles in a stirred tank

In semi-batch precipitation processes, the particle size distribution and quantity of solid particles may differ over time, which may also affect other phenomena taking place during precipitation. In the heterogeneous reactive crystallization occurring in a gas-liquid system, absorption is one of the unit operations. Tiny nuclei may first form during precipitation. The existence of these small particles may have an impact on the absorption rate, and therefore, the influence of solid particles on absorption was investigated (Han et al. 2011, Sha et al. 2015).

4.1 Introduction

Mass transfer of gas-liquid (G-L) systems is crucial in a number of chemical unit operations, such as heterogeneous reactive crystallization, hydrogenation, oxidation, and chlorination. To enhance gas-liquid mass transfer, bubble size should be sufficiently small to maximize the interfacial surface area and gas bubbles should be dispersed into the continuous liquid phase as uniformly as possible. The mass transfer coefficient in a gas-liquid system is usually expressed by a volumetric mass transfer coefficient, k_{LA} , which is an important parameter for the design of reactors, their scale-up and unit operations. The volumetric mass transfer coefficient is affected by many factors, such as the undersaturation level of the absorbing gas compound in the solution (driving force), gas holdup, bubble size distribution, temperature, pressure, agitation, gas flow rate and liquid viscosity.

4.1.1 Mechanism of mass transfer of absorption at gas-liquid interfaces

Gas absorption in the liquid phase can be divided into two kinds of processes. One is physical absorption involving molecular and convective transport of atoms and molecules within the physical system. The other is chemical absorption in which a reaction between the gas and liquid phases takes place. Often, chemical species transfer between the two phases through an interface or diffusion. The driving force of mass transfer processes is the concentration difference between the phases. The random motion of molecules causes a net transfer of mass from an area of high concentration to an area of low concentration. For separation processes, thermodynamics shows the equilibrium state which the system intends to achieve, while mass transfer models can yield the rates at which the separation will occur, and the fluxes of transferring compounds. There are many widely used mass transfer theories such as the double boundary layer model, Higbie penetration theory, Danckwerts surface renewal model and combinations of these theories. (Zlokarnik 2001)

4.1.2 Effect of solids on the mechanism of mass transfer of absorption

According to Cooke et al. (2008) three main mechanisms of gas-liquid mass transfer are influenced by solids. Firstly, the apparent viscosity of the solid-liquid suspension can be affected due to damping of the turbulence by solids. Secondly, in the heterogeneous

regime, solids have been shown to supplant small bubbles in the dense phase, which will affect gas-liquid mass transfer. Cooke et al. (2008) studied in detail if this mechanism explains results indicating a decrease in gas-liquid mass transfer with solid addition. They found that the addition of solids can reduce gas hold-up, and thus decrease the gas-liquid mass transfer in an air-water system. However, in a Na_2SO_4 system both large and small bubbles coalesced due to the presence of solid particles. This is a different mechanism than that previously proposed of solids simply supplanting small gas bubbles out of the dense phase. Thirdly, there can be an interface effect: very tiny active particles acting at the interface enhance the gas-liquid mass transfer (Kordač and Linek, 2006) or cause a very large reduction in gas-liquid mass transfer by inducing coalescence. Gentile et al. (2003) reported that the non-wetted particles tend to collect at the air-water interface and bridge the dividing water film between the bubbles, which enhances the coalescence.

Relating to the enhancement of gas-liquid mass transfer rate, four mechanisms are introduced in the literature (Ruthiya et al. 2003a, 2003b, Kluytmans et al., 2003). I. Boundary layer mixing. Four different physical phenomena influence the convective mass transfer and the concentration gradient at the G-L interface. II. Shuttling. Visiting frequency of particles at the G-L interface is increased by increasing solid concentration and mixing intensity. This leads to an increased transport of gas from the G-L interface to the bulk liquid and thus an increase in k_L . For instance, Kordač and Linek (2006) reported that the interface is rigid in the absence of particles, which hinders the motion of liquid along the interface, forming a boundary layer; whereas in the presence of particles, the interface is completely mobile and surface renewal proceeds according to the penetration model. III. Coalescence inhibition. In a suspension, particles adhering to bubbles and electrolyte can reduce or hinder the coalescence of gas bubbles, which results in an increase in the G-L interfacial area. The following five factors can affect this mechanism: surface tension of the liquid, viscosity and density of the liquid or suspension, ionic forces, lyophobicity of the particles, and particle size. Kluytmans et al. (2003a, 2001) presented that the gas-liquid interfacial area was increased by the addition of carbon particles and electrolytes in a bubble column and stirred tank reactor with the gas inducing impeller. IV. Boundary layer reaction or grazing effect. When fine particles catalyze a chemical reaction at the G-L interface, significant conversion occurs within the diffusion layer around the gas bubbles, therefore increasing the mass transfer rate. This explains the enhancement of mass transfer with catalyst particles (Zhang et al., 2006, 2008).

4.1.3 Factors affecting mass transfer of absorption

The presence of solid particles can influence several ways in gas-liquid systems, such as mass transfer rates, gas holdup, and bubble size distribution. The mass transfer rate between gas and liquid is affected by the density difference between the solid and liquid, the volume fraction of solids in the suspension, and the particle size. Larger particles can enhance the mass transfer rate by increasing eddy generation and by breaking gas bubbles. On the other hand, the presence of small particles can reduce the mass transfer rate, as the small particles may influence fluid rheology by decreasing the apparent viscosity of the suspension. This effect can be a crucial factor in semi-batch precipitation, where very

small nuclei are usually formed (He et al. 2006, Yuan and Murray 1997, Willoughby and Sharma 2004, Sudduth 2008).

Generally, mass transfer of absorption in stirred tanks is accelerated by increasing the gas flow rate, mixing intensity, temperature, etc. (Ferreira et al. 2010, Gómez-Díaz et al. 2003, 2005, Velts et al. 2010). In addition, solid properties and quantity are important. Ferreira et al. (2010) investigated the effect of solid phase properties (size and density) on the gas-liquid mass transfer characteristics and their respective physical properties at different temperatures in a bubble column. They concluded that the solid size and loading have a negative effect on k_{La} . The k_{La} was increased with increase in temperature. An empirical correlation for k_{La} dependence on the experimental variables was developed. Mena et al. (2011) studied whether solid concentration and solid particle properties such as mean diameter affect k_{La} in a bubble column. The results showed that the k_{La} decreased with increasing solid loading and mean diameter. The loading of hollow glass spheres had a dual effect on k_{La} . Namely, for low solid loading k_{La} increases with solid content and decreases with further solid addition. This effect relates to different surface particle properties.

Few studies, however, have investigated the influence of different-sized particles on mass transfer in stirred tanks or reactors. Since mechanically agitated vessels are widely used for gas-liquid reactions, for example, in waste disposal plants and in fermentation, the absorption processes affected by solid particles in a stirred tank is a valid and important area of research. Findings from such work would provide very useful information for vessel design and optimization of unit operations.

4.2 Experimental section

4.2.1 Experimental material

Sieved solid particles, quartz and calcium carbonate were used to investigate their influence on mass transfer of oxygen in the compared air and tap water system. The particle size distribution of the sieved particles was analyzed by a Beckman Coulter LS 13320 laser diffraction particle size analyzer. The results are shown in Figure 4.1. The median diameters of the two different quartz particles are 640 μm (Fig. 4.1a) and 41.1 μm (Fig. 4.1b) respectively. The median diameter of the calcium carbonate particles was 5.07 μm (Fig. 4.1c).

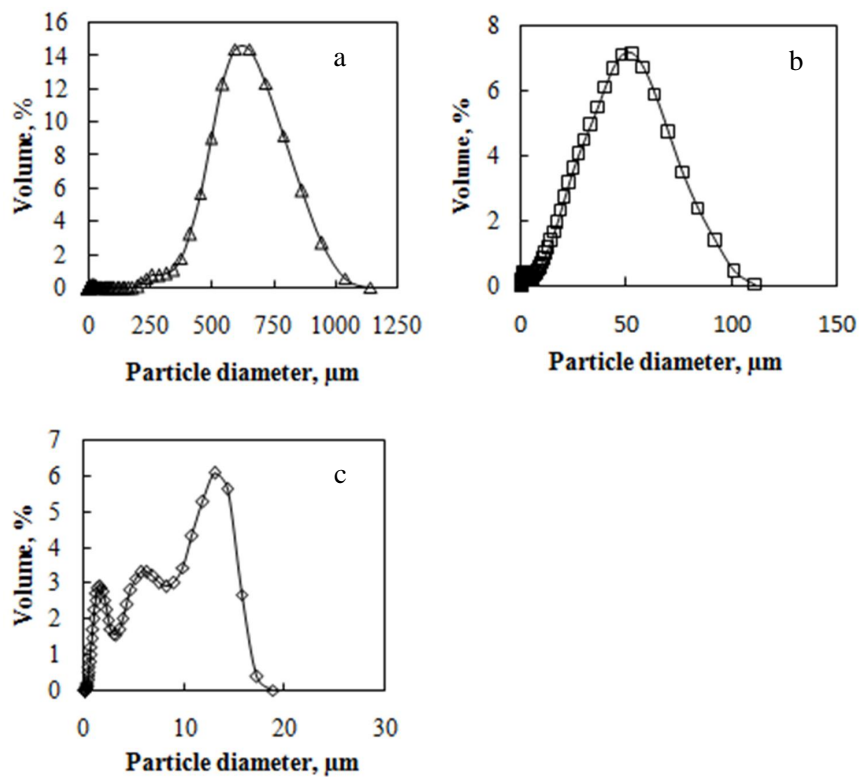


Figure 4.1 Particle size distribution of quartz (a, b) and calcium carbonate(c).

4.2.2 Experimental method

Experimental procedure

Experiments were carried out in an acrylic glass tank with a diameter and height of 0.48 m and 0.60 m, respectively. Four baffles (1/10 of the vessel diameter width) were installed symmetrically on the inner wall of the tank to promote mixing. A Rushton stirrer of 0.16 m diameter was used for mixing. The stirrer was located 0.16 m from the bottom of the tank.

The physical absorption system was studied using oxygen absorption into water and solid-liquid suspensions in the present work. In each experiment, approximately 87 liters of tap water were first fed into the tank. The temperature of the solution was adjusted by an immersed coil, which was connected to a thermostat. This coil was removed after reaching the target temperature in order to ensure that it did not affect the flow pattern. All absorption experiments in this study were carried out at 10 °C because generally the solubility of gases in liquids is higher at low temperatures. A probe of an oxygen meter (Marvet Basic 2000, Elke Sensor LLC) was immersed in the tank to monitor the concentration of dissolved oxygen in the solution. The probe recorded data every 6 s. A certain amount of solid was added and mixed in the tank for 10 min in order to disperse

the particles well. A dynamic gassing-out method was used (Van't Riet 1979). Nitrogen was used to remove the oxygen in the system. When the saturation level achieved less than 5 %, pressurized air was fed into the water through a sparger at the bottom of the tank and distributed by a Rushton stirrer. The experiment was ended when the saturation level reached 95 %. A superficial gas velocity of 5.5×10^{-4} m/s and various rotation speeds were used for all experiments. The mixing power was measured by a torque meter. The schematic system of the experiment is shown in Figure 4.2.

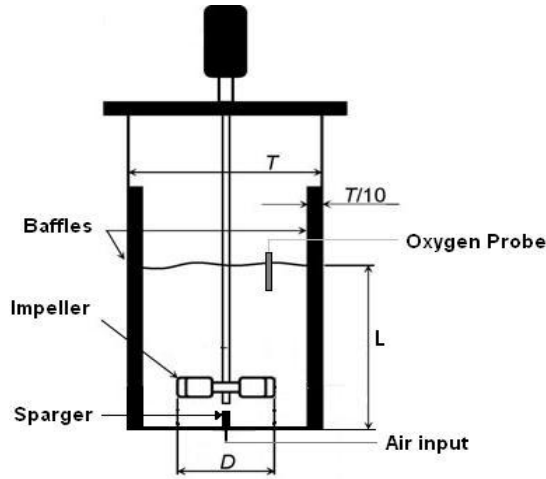


Figure 4.2 Schematic of the experimental set-up (Sha et al. 2015).

Calculation of critical impeller speed

Mixing of gases and solids in liquids in mechanically agitated reactors is employed in 80 % of chemical industry operations; such operations include leaching, complete dissolution of reagents, and suspension of catalysts and products such as precipitates and crystals (Smith 1990). Agitation can increase the contact area between phases through mixing, so it is widely used in unit operations. In general, a dispersion of the suspension is considered to be complete if no particle remains at rest at the bottom of the vessel for more than 1 or 2 s. This chapter mainly considers a gas-liquid-solid three phase system, which means that agitation is important. In order to reach complete suspension, the critical rotation speed of the impeller needs to be calculated.

The most commonly used critical impeller rotation speed is that of Zwietering (1958), who proposed a correlation for minimum impeller speed for complete suspension of solids based on a huge amount of experimental data. The equation is shown in Eq. (4.1):

$$N_{js} = \frac{Sv^{0.1} d_p^{0.2} \left(\frac{g(\rho_p - \rho)}{\rho} \right)^{0.45}}{D^{0.85}} X^{0.13} \quad (4.1)$$

where N_{js} is the critical impeller speed for solids, rpm; S the impeller constant depending on the ratio of the impeller to diameter of reactor (in this study, $S=7.5$ for the Rushton impeller); ν the kinematic viscosity, $\text{m}^2 \text{s}^{-1}$; d_p the average particle diameter, m; ρ_p and ρ the particle density and liquid density, respectively, kg m^{-3} ; X the mass ratio of suspended solids to liquid $\times 100$, $\text{kg solid/kg liquid} \times 100$; D the diameter of the impeller, m; and g the gravity acceleration, m s^{-2} .

In gas-liquid-solid and liquid-solid reactors, critical speed depends on many factors such as particle settling velocity, design of the impeller and sparger, and their positions. Using empirical Eq. (4.1), researchers (Chapman et al., 1983, Nienow et al., 1986, Wong et al., 1987, Rewatkar et al., 1991, Dylag et al., 1994) have suggested different critical impeller speeds for gas-liquid-solid phases based on reactor and impeller type. Eq. (4.2) was used to calculate critical impeller speed in the present study for three phase system (Chapman et al., 1983).

$$N_{jsg} = N_{js} + 0.94Q_v \quad (4.2)$$

where N_{jsg} is the critical impeller speed for gas-liquid-solid system, rpm; Q_v the ratio of gas flow rate to liquid volume, $\text{m}^3/(\text{m}^3 \text{ min})$.

Table 4.1 shows the basic data used for calculating the critical impeller speed. The critical impeller speed for the solid suspension density and operating conditions used in the present study is listed in Table 4.2. Several absorption experiments were carried out with the rotation speeds in the range of 220-470 rpm, namely $3.67\text{-}78.33 \text{ s}^{-1}$.

Table 4.1 Basic data for calculating critical impeller speed.

Property Solid	ρ (kg/m^3)	ν (m^2/s)	d_p (m)
water	999.7	1.31×10^{-6}	-
quartz	2650	-	4.11×10^{-5}
quartz	2650	-	6.40×10^{-4}
calcium carbonate	2710	-	5.07×10^{-6}

Table 4.2 Critical impeller speed with various solid volume fractions at constant superficial gas velocity ($5.5 \times 10^{-4} \text{ m/s}$).

Critical rotation speed, rpm	Solid volume fraction, %						
	0.01	0.03	0.08	0.38	1.00	2.17	3.56
quartz (640 μm)	267	320	360	444	506	560	599
quartz (41.1 μm)	155	185	208	257	292	324	346
CaCO_3 (5.07 μm)	103	124	139	171	195	216	231

Calculation of volumetric mass transfer coefficient k_La

As reported by Fuchs et al. (1971), Van't Riet (1979), and Vandu and Krishna (2004), the signal measured by the oxygen probe has an inherent delayed response. This lag time has to be considered in the mass transfer data treatment in order to guarantee the accuracy of the transfer rate. In order to obtain the probe response time τ , the probe of the oxygen meter was swiftly transferred from water completely desorbed of oxygen content to a 100 % oxygen saturated water solution. The abrupt rise in the oxygen meter reading was monitored and recorded at 6 s time intervals. The dynamic response curve of the oxygen sensor is shown in Figure 4.3. Subsequently, the probe response time τ was determined by recording 63.2 % of the step change. According to five measurement results, the response time was 31 s.

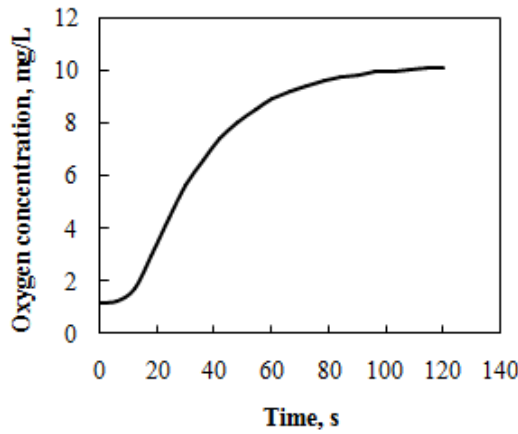


Figure 4.3 Dynamic response of oxygen sensor obtained by calculating response time.

The volumetric mass transfer coefficient, k_La , can be calculated from the concentration against time t by Eq (4.3) using a statistical method (Fuchs et al. 1971).

$$C = C^* - \frac{C^* - C_0}{\tau^{-1} - k_La} \left(\tau^{-1} e^{-k_La \cdot t} - k_La \cdot e^{-t/\tau} \right) \quad (4.3)$$

where C^* and C_0 are the oxygen solubility and oxygen concentration at $t = 0$, respectively; and C is the concentration of oxygen in the liquid. Figure 4.4 shows the experimental data points of oxygen concentration versus time and a fitting curve by Eq (4.3) for the air-water system with a gas velocity 5.5×10^{-4} m/s and rotation speed 3.93 s^{-1} at 10°C . Each experiment was repeated two or three times under the same conditions in order to obtain accurate experimental data.

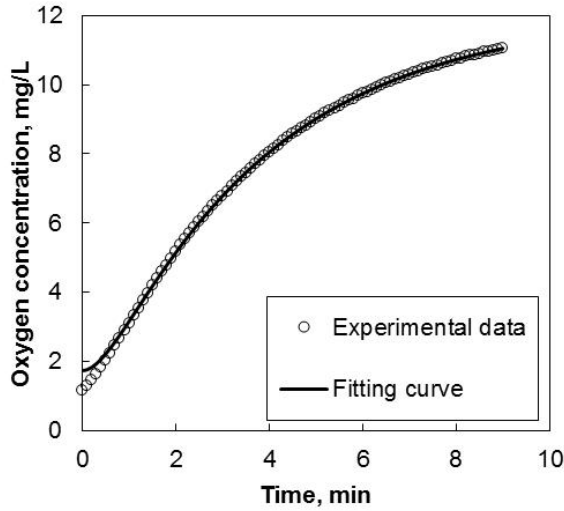


Figure 4.4 Dissolved oxygen concentration versus time for an air-water system with the superficial gas velocity of 5.5×10^{-4} m/s and rotation speed of 3.93 s^{-1} at 10°C (Sha et al. 2015).

4.3 Results and discussion

4.3.1 Absorption of oxygen to water in an air-water system

Before studying the influence of solid particles on mass transfer between the gas and liquid phase, mass transfer experiments in an air-water system were performed. In general, volumetric mass transfer coefficient ($k_L a$) is expressed as a function of specific power input (P_G/V_L) and superficial gas velocity (u_g), as according to Eq (4.4).

$$k_L a = \kappa \left(\frac{P_G}{V_L} \right)^\alpha (u_g)^\beta \quad (4.4)$$

The parameters of κ , α and β are determined based on the experimental conditions. The exponents obtained from the present work with literature data (Van't Riet 1979, Juárez and Orejas 2001, Stenberg and Andersson 1988, Linek et al. 1991, Wu 1995, Moucha et al. 1995, Linek et al. 1987, Smith et al. 1977) are summarized and compared in Table 4.3. Because constant gas flow rate is used in the current study, it is impossible to get the exponent value of β . However, it can be seen that the value of α is in the reasonable range proposed by former data.

Table 4.3 Comparison of mass transfer correlation constants for an air-water system between literature data and the present work (Sha et al. 2015).

Reference	Mass transfer coefficient $k_{La} = \kappa(P_g/V_L)^\alpha(u_g)^\beta$		
	κ	α	β
Van't Riet 1979	0.026	0.4	0.5
Juárez et al. 2001	0.00111	0.9504	0.6282
Linek et al. 1987	0.00495	0.593	0.4
Linek et al. 1991	0.00384	0.654	0.4
Moucha et al. 1995	0.0146	0.611	0.554
Smith et al. 1977	0.0104	0.475	0.4
Wu et al. 1995	0.01036	0.67	0.56
Stenbergand Andersson, 1988	0.0053	0.55	0.32
This work	0.3571	0.488	—

4.3.2 Influence of quartz particles on absorption mass transfer of oxygen in an air-water system

The measured results of the volumetric mass transfer coefficients in the air-water system in the presence of quartz sands are shown in Figure 4.5. The values show that the volumetric mass transfer coefficient increased with increasing specific power input both with and without particles in the system. Simultaneously, there was no effect of quartz sands on gas-liquid mass transfer with solid volume fraction ε_s from 0.01 to 0.08 % (solid mass fraction $w_s = 0.02$ to 0.2 %) and two sizes of quartz particles. This result is the same as the findings obtained by Alper et al. (1980), ($w_s = 0$ to 2 %), but different from the results by Oguz et al. (1987) who reported that k_{La} decreased with increasing volume fraction of solid phase in the range of 0.01 to 0.1. Therefore, the main factor of k_{La} is not affected by the quartz quantity alone, i.e. suspension density, but also by other experimental conditions, such as the gas flow rate.

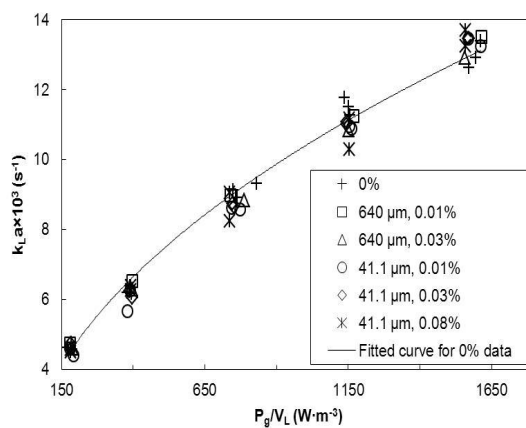


Figure 4.5 Effect of quartz sands with different volume fractions on the absorption mass transfer of oxygen from air to water in a stirred tank with a superficial gas velocity of 5.5×10^{-4} m/s at 10 °C (Sha et al. 2015).

4.3.3 Influence of calcium carbonate particles on the absorption mass transfer of oxygen in an air-water system

The determined results of mass transfer between air and water with the presence of CaCO_3 particles are shown in Figure 4.6. The values show that the volumetric mass transfer coefficient increased with specific power input as reported in the literature. The volumetric mass transfer coefficient k_{La} in the studied system is dependent on the concentration of the particles in the suspension. When the concentration of CaCO_3 particles in the suspension is below 10 kg/m^3 ($\varepsilon_s = 0.4 \%$), the particles have no obvious effect on k_{La} . When the solid loading is higher than 0.4% , the volumetric mass transfer coefficient starts to increase.

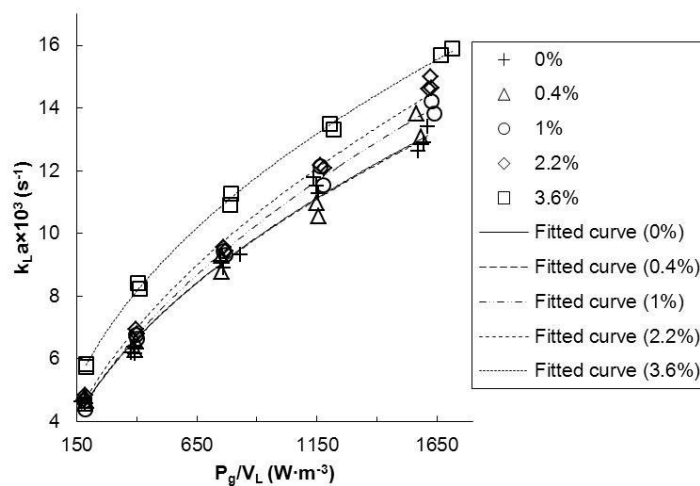


Figure 4.6 Effect of CaCO_3 particles with different volume fractions on the mass transfer of oxygen from air to water in a stirred tank with a superficial gas velocity of $5.5 \times 10^{-4} \text{ m/s}$ at 10°C (Sha et al. 2015).

In order to find the reason for the increase in the volumetric mass transfer coefficient in the presence of calcium carbonate particles, viscosities of different suspended solutions were measured at 10°C and 25°C using a MCR Anton Paar rheometer (cylinder chamber). The results are shown in Table 4.4. A dynamic viscosity increase can be expected to increase the mass transfer resistance thus leading to lower k_{La} value.

Table 4.4 Dynamic viscosity of calcium carbonate slurry with various volume fractions at 10°C and 25°C

Volume fraction of CaCO_3 in slurry (%)	Viscosity ($\times 10^{-3} \text{ Pa s}$)	
	10°C	25°C
0.4	1.3	1.2
1.0	1.3	1.2
2.2	2	1.4
3.6	2.3	1.9

From Table 4.4, it can be seen that the viscosity of the slurry decreases with increasing temperature, as commonly known, and increases because of the presence of CaCO_3 particles of $5.07\ \mu\text{m}$ at constant temperature. Moreover, the viscosity of the suspension rises slightly with the addition of CaCO_3 crystals: the thicker suspension had a higher viscosity. However, the viscosity of the suspension with suspension density of $96.4\ \text{kg/m}^3$ ($\varepsilon_s = 3.6\%$) was still quite low. The viscosity of the CaCO_3 suspension was only 2.3 times higher than that of pure water at $10\ ^\circ\text{C}$. The suspensions at the studied suspension densities were found to be Newtonian fluids (obtained dynamic viscosity values approximately constant at shear rates of 10 to $100\ \text{s}^{-1}$).

Generally, the viscosity of a solid-liquid suspension is higher than the viscosity of pure water. This results in decreased gas bubble spreading in the reactor and promotion of gas bubble coalescence leading to lower values of gas-liquid mass transfer coefficient k_L and gas-liquid interfacial area a , respectively (Li et al., 1996). In the present study, however, according to Figure 4.6, k_{LA} increased with increasing suspension density of CaCO_3 , from 10 to $96.4\ \text{kg/m}^3$ ($\varepsilon_s = 0.4 - 3.6\%$). The presence of solid particles in the stirred tank was expected to affect the hydrodynamics and consequently the gas-liquid mass transfer process. At low suspension density, a small amount of solid particles cannot have a strong effect, and thus the difference in k_{LA} between the absence and the presence of solid particles is not great. When the content of CaCO_3 crystals is increased, the particles play a role in the gas-liquid mass transfer that is larger than the effect of viscosity. It means that the frequency of the surface renewal and interface mobility are increased and the bubble coalescence inhibited, as discussed by Ruthiya et al. (2003b). Particles adhering to the gas bubbles in the suspension can reduce or hinder gas bubble coalescence. Thus, in the presence of small particles the total gas-liquid interfacial surface area is greater than the total surface area in clear liquids, i.e. the bubbles remain smaller, which increases the volumetric mass transfer coefficient.

4.3.4 Gas-liquid mass transfer model in the presence of solids

As discussed above, the studied factors such as specific power input, particle size, and solid content have an impact on the mass transfer rate of absorption. Obtained experimental results were fitted using the function $k_{LA} = f(P_g/V_L, \mu^*, d_p, \varepsilon_s)$. Some researchers have proposed empirical models of mass transfer coefficient with the existence of particles in a stirred reactor (Linek et al., 2008, Kielbus-Rapala and Karcz, 2009). However, in the stirred tank gas-liquid mass transfer model considering both solid concentration and particle size has not been published.

Although two solids were studied in the current work, their densities are similar to each other (Table 4.1). Thus this study could be considered as describing the impact of different-sized particles of the same solids on gas-liquid mass transfer rate. Based on the 103 experimental data points for different-sized solid particles and various solid loading at constant superficial gas velocity of $5.5 \times 10^{-4}\ \text{m/s}$, the following correlation was obtained:

$$k_L a = 46.1 \left(\frac{P_G}{V_L} \right)^{0.494} (\mu^*)^{1.78} (1 - d_p)^{-0.0056} (1 - \varepsilon_s)^{-0.739} \quad (4.5)$$

where μ^* is the effective dynamic viscosity of the particle-liquid mixture and d_p is the particle size. μ^* can be determined by Einstein expression (Coulson et al., 2002) shown in Eq (4.6).

$$\mu^* = (1 + 2.5\varepsilon_s)\mu_L \quad (4.6)$$

where μ_L is the viscosity of the liquid. This expression is very useful for gas-liquid-solid three phase systems because the volumetric concentration of the particles has an influence on the viscosity of the system, which may affect the interfacial area.

A comparison of the experimental data and values obtained from Eq. (4.5) is presented in Figure 4.7. It can be seen that the predicted results agree quite well with the experimental results. The average relative error is 3.16 %. The form of the correlation reflects that the absorption rate is mainly influenced by specific power input, effective viscosity of the system and solid loading. The particle size does not affect it as strongly.

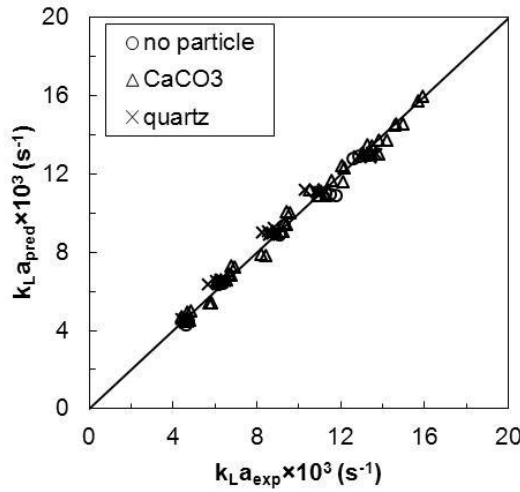


Figure 4.7 Comparison of the experimental results ($k_{La_{exp}}$) and the predicted results ($k_{La_{pred}}$) calculated from Eq (4.5) (Sha et al. 2015).

4.4 Summary

The effect of solid particles on absorption mass transfer of oxygen for an air-water system in a stirred tank was studied experimentally. At a constant temperature of 10 °C and gas flow rate of 5.5×10^{-4} m/s, the volumetric mass transfer coefficient k_{La} increased with the increase in specific power input. Quartz sand particles with mean size of 41.1

and 640 μm did not have an impact on k_{LA} with solid volume fraction up to 0.08 %. However, CaCO_3 particles of 5.07 μm were found to have an effect on k_{LA} . This effect depended on the solid content in the system. There was almost no effect of CaCO_3 particles on the mass transfer rate for solid volume fraction of 0.4 %. However, k_{LA} increased with the addition of a larger amount of CaCO_3 particles when the solid volume fraction range varied from 1 to 3.6 %. The obtained correlation expression for the volumetric mass transfer coefficient k_{LA} in the studied stirred tank system is shown in Eq (4.5). However, the applicability of this equation is limited to the conditions used in the current study. Generally, many parameters such as gas flow rate, geometry of reactor and impeller, surface tension, temperature and solid type have an impact on the mass transfer rate. To summarize, the influence of solids on gas-liquid mass transfer cannot be ignored in a multiphase system such as the gas-liquid reaction crystallization process. It was evidenced by the experimental results that the presence of small particles smaller than 10 μm in volume fraction range below 4 % may have an effect on the mass transfer rates of absorption in semi-batch precipitation processes where the crystal size distribution may change over time due to nucleation and crystal growth. Absorption rates can be higher with high nucleation rates and suspension densities.

5. Application of Raman spectrometry to anti-solvent precipitation and evaporation crystallization

This section introduces the studies carried out when Raman spectrometry was used for inline and offline analysis of anti-solvent precipitation of KDP and evaporation crystallization with aqueous and organic compound systems. Application of Raman analysis for monitoring of reactive crystallization of magnesium carbonate was discussed in Chapter 3 above.

5.1 Anti-solvent precipitation of potassium dihydrogen phosphate (Publication I)

Raman spectrometry was used for inline measurements to real-time monitor semi-batch anti-solvent precipitation of KDP with acetone from aqueous solution.

5.1.1 Introduction

Anti-solvent precipitation is defined as a solute crystallized from a primary solvent by the addition of another solvent in which the solute is relatively insoluble. The solubility of the solute decreases due to the existence of the second solvent. Anti-solvent crystallization is a powerful isolation and purification technique, especially for systems where the temperature coefficient of solubility is low or the solute is unstable at elevated temperatures (O'Grady et al. 2007). For instance, the technique is commonly used for crystallization processes of pharmaceutical compounds.

One of the advantages of anti-solvent crystallization is that precipitation can be carried out at low temperature, which is important for thermally sensitive products. Consequently, the approach is energy-efficient compared with evaporation crystallization. Another advantage is that the solvent activity changes remarkably, so the method can have more profound effect on the crystal shape or polymorphic form than in the case of the cooling crystallization. However, anti-solvent crystallization also has disadvantages. The solvent separation or recycling incurs additional costs. Higher capital costs are also required due to the high supersaturation gradients needed in large scale systems (Mostafa Nowee et al., 2008, Nagy et al., 2008). On the other hand, the anti-solvent crystallization approach is highly dependent on mixing. When poor mixing regimes exist, high local supersaturation occurs at antisolvent induction zones. This results in excess primary nucleation rates, which leads to fine crystal particle formation that easily tends to agglomerate. (Takiyama et al. 1998)

Various parameters have effects on anti-solvent crystallization. Such parameters include mixing intensity, seeding, addition rate and concentration of the anti-solvent, which all have an impact on nucleation and crystal growth because of the resultant changes in the driving force supersaturation. Crystal shape and size are thus affected by these operating factors (Kim et al., 2003, Kitamura and Sugimoto, 2003, Yu et al., 2005, Zhang et al., 2010, Lee et al., 2014). Increasingly advanced technologies have been used to monitor

anti-solvent crystallization, and real-time information has become available that can assist in control of this complex process. Anti-solvent crystallization of cortisone acetate was in situ monitored by fiber optic Raman spectrometry by Falcon and Berglund (2003). Their results showed that Raman spectrometry can monitor both the solution phase, i.e. the mother liquor, and the solid state form. Yu et al. (2006) investigated the effects of seed loading and seed size distribution on anti-solvent crystallization of paracetamol from a water-acetone mixture operated at constant supersaturation by attenuated total reflectance Fourier transform infrared (ATR-FTIR) spectroscopy. A focused beam reflectance measurement (FBRM) probe was used to in-situ measure solid phase information such as chord length distribution. Brown et al. (2011) studied anti-solvent crystallization (acetone/water system) of paracetamol in an oscillatory baffled crystallizer. The mass of crystals were tracked in time by laser illuminated video imaging. This analysis method allowed determination and monitoring of the instantaneous and overall average rate of crystal mass growth. Zhang et al. (2011) showed the feasibility of ultraviolet fiber spectroscopy for on-line concentration measurement of anti-solvent crystallization (ethanol/water system) of β -artemether. The results indicated that the dependence of temperature on UV spectra was weak, but UV spectra were related to the β -artemether concentration and the solvent composition. Moreover, application of attenuated total reflectance ultraviolet visible (ATR-UV/vis) spectroscopy for the monitoring of a multi-component crystallization system with FBRM has been reported (Saleemi et al., 2012). The predicted concentration profiles by the developed model using principal component artificial neural networks agreed quite well with the actual data. These process analytical technological tools provide valuable information, including the identification of compounds and monitoring of their respective concentrations in the solution.

5.1.2 Experimental section

The anti-solvent crystallization of KH_2PO_4 at 25 °C was on-line monitored by Raman spectroscopy, where water and acetone were used as the solvent and anti-solvent respectively. First, the solubility of KH_2PO_4 in water with various mass fraction of acetone was experimentally determined by gravimetric method. A function of KH_2PO_4 solubility and concentration of acetone was obtained and used in the further calculation of KH_2PO_4 solubility at different concentrations of acetone at 25 °C (Publication II). A calibration model was needed to correlate the Raman spectra with the KH_2PO_4 concentration in the solution. Therefore, 13 ternary undersaturated solutions were used to generate the Raman calibration model. Beckman Coulter LS13320 laser diffraction particle size analyzer was used to determine particle size distribution of precipitates. Detailed methodology descriptions, such as experimental set-up, measuring procedure and the calibration approach are introduced in Publication I.

5.1.3 Results and discussion

Six semi-batch anti-solvent crystallization experiments with two feeding positions and three feeding rates were carried out. The concentration profiles over time obtained from

the predicted and experimental results are shown in Fig. 5.1 to 5.4. The other two graphs were presented in Publication I.

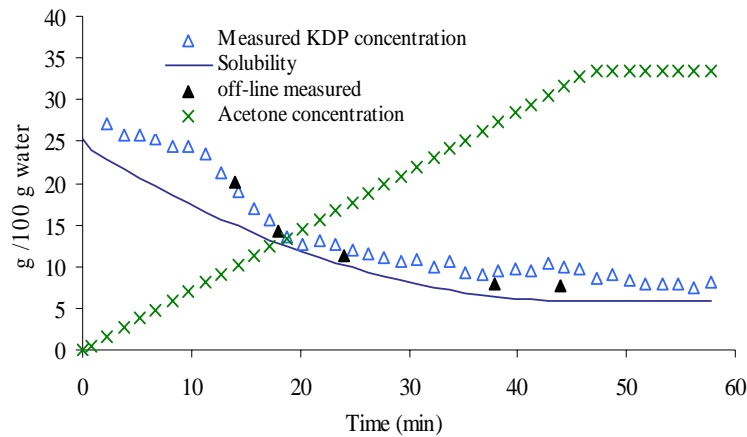


Fig. 5.1 Obtained KDP and acetone concentration profiles for batch time of 47 min, feed up.

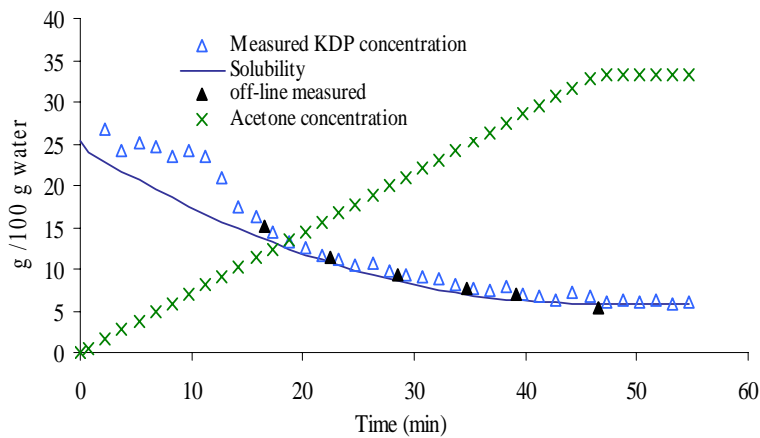


Fig. 5.2 Obtained KDP and acetone concentration profiles for batch time of 47 min, feed down.

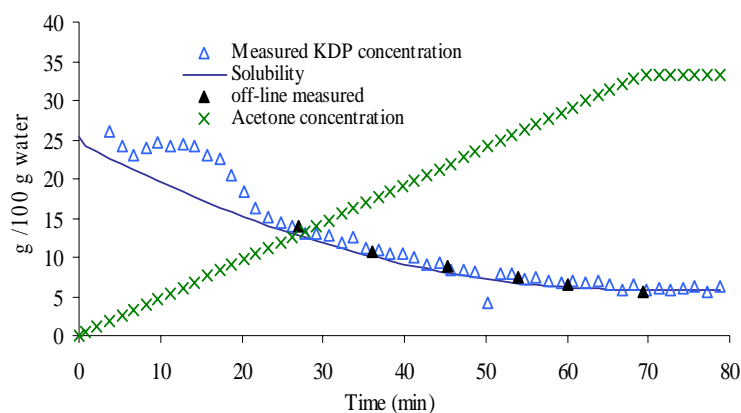


Fig. 5.3 Obtained KDP and acetone concentration profiles for batch time of 69 min, feed down.

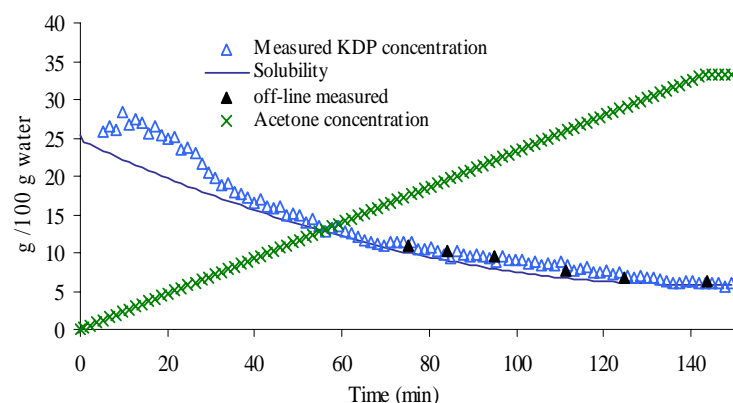


Fig. 5.4 Obtained KDP and acetone concentration profiles for batch time of 137 min, feed down.

All the figures show that a similar trend was observed with different feeding rates and feeding positions. Two feeding positions that near the surface of the crystallizer and close to impeller were named feed up and feed down respectively. The concentration of KDP in the solution determined by the Raman calibration model agreed well with the concentration measured off-line by gravimetrical method. With the addition of acetone in the system, KDP concentration initially maintained a constant level, then quickly dropped and reduced gently at the end. The profile indicates three periods: an induction, nucleation and crystal growth period (Jiang et al. 2004). The driving force, supersaturation, increased to a maximum level, then sharply decreased, and finally maintained a constant level. The supersaturation profiles are shown in Fig. 5.5a and 5.6a. For both feeding positions, the supersaturation increased with increase in the feeding rate of acetone. Particle size

distribution of the final product, shown in Fig. 5.5b and 5.6b, reduced with increasing feeding rate due to the higher supersaturation generated.

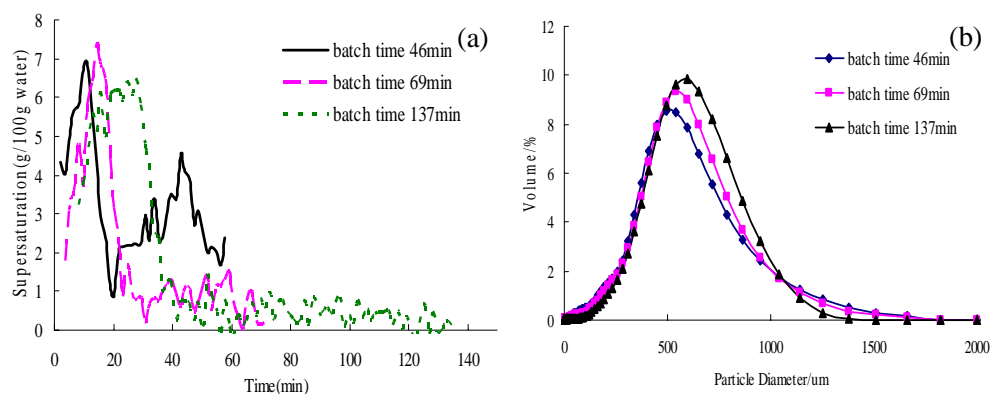


Fig. 5.5 Supersaturation profile (a) and crystal size distribution (b) of KDP with feed up.

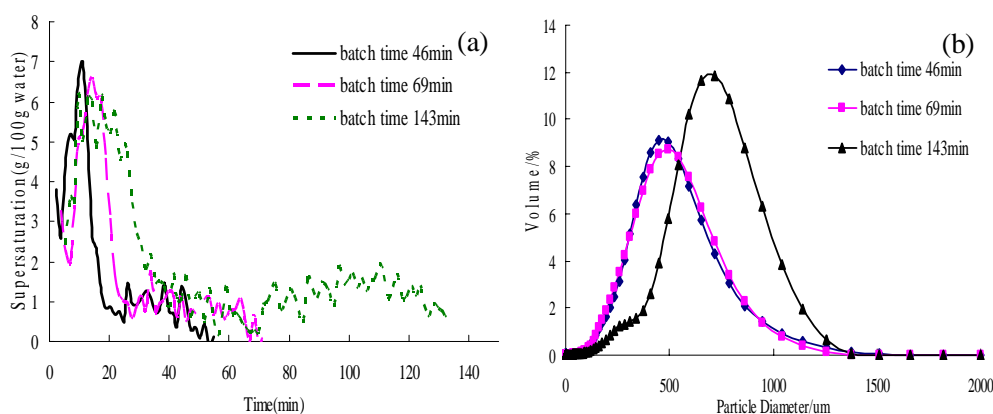


Fig. 5.6 Supersaturation profile (a) and crystal size distribution (b) of KDP with feed down.

When comparing the supersaturation profiles for the two feeding positions shown in Fig. 5.7, Fig. 5.8 and Publication I, no significant difference is observed with the studied feeding positions of acetone. This means that mixing is efficient and the concentration in the reactor can be considered as being uniform.

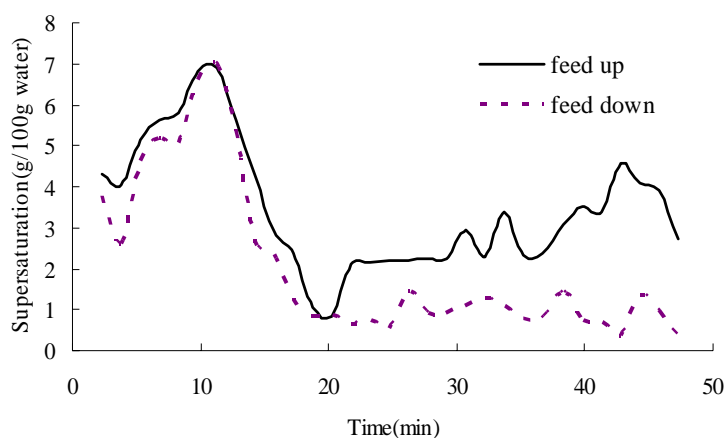


Fig. 5.7 Supersaturation of KDP with two feeding positions with batch time of 46 min.

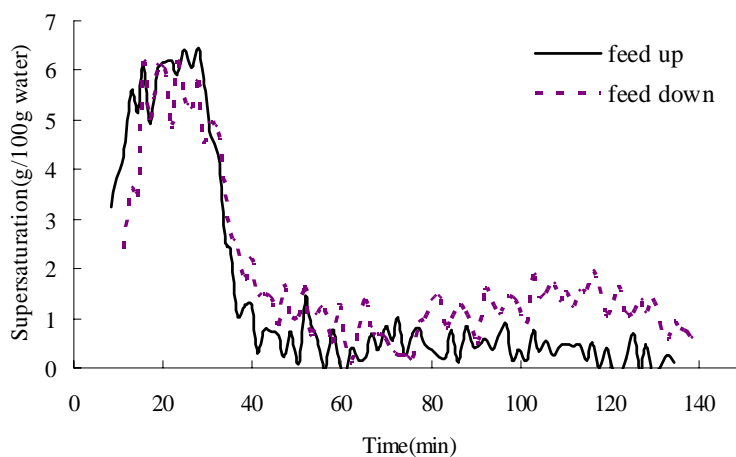


Fig. 5.8 Supersaturation of KDP with two feeding positions with batch time of 137 min.

5.2 Evaporation crystallization of indomethacin solutions (Publication III)

As described in this section of the present work, Raman spectrometry was used for offline polymorphs and solvates analyses of indomethacin crystals obtained by evaporation crystallization with various solvents.

5.2.1 Experimental section

Evaporation crystallization experiments of indomethacin (IMC) from pure organic solvents such as ethanol, acetone and ethyl acetate were carried out at ambient temperature and pressure. The polymorphs of obtained IMC were determined offline with

Raman spectroscopy. Detailed description of the experimental materials and procedure is introduced in Publication III.

5.2.2 Results and discussion

It was found that the predicted evaporation rates for acetone and ethyl acetate calculated with a mathematic model based on Fick's first law of diffusion and a hypothesis of one component mass transfer from the liquid surface through the stagnant gas phase (McCabe et al. 2005) agreed well with the experimental results. However, the predicted value for ethanol was about 36 % lower than the experimental result. Accelerated flux caused by the surrounding airflow might be a reason for the discrepancy since the evaporation rate is very sensitive to the ventilation surrounding the experimental system.

Raman analysis showed that α -IMC was formed for ethanol and ethyl acetate at the characteristic peak of 1650 cm^{-1} during evaporation as seen in Publication III Fig. 5. There is a remarkable peak at Raman shift of 1690 cm^{-1} for boundary layer 3 cm. Two characteristic peaks at wavenumber of 1650 cm^{-1} and 1690 cm^{-1} appeared for boundary layer 4 cm. Consequently, both α and the solvate form of IMC can be obtained from the evaporation process when acetone is used as a solvent (Fig. 6 in Publication III). All the main outcomes were shown and discussed in Publication III.

5.3 Summary

Raman spectroscopy could successfully monitor the precipitation process of KDP with acetone as the anti-solvent. The concentration of KDP could be predicted by the calibration model and the supersaturation of KDP could thus be determined. The results showed that the feeding rate of acetone had an effect on the crystal product: the higher the feed rate, the smaller the crystal size. However, feeding position had no obvious influence on the crystallization.

The mathematic mass transfer model successfully predicted the flux and the evaporation rate of solvent during evaporation. Offline measurement by Raman spectroscopy can easily identify the polymorph of indomethacin. Therefore, Raman spectroscopy is a powerful analytical tool that can not only determine the polymorph of compound, but also provide real-time information, which is very important and valuable for better controlled crystallization processes.

6. Conclusions

The present work focused on study of multi-phase phenomena and crystallization kinetics in various crystallization processes using advanced process analytical technology. Phenomena having an impact on gas-liquid reactive crystallization and related to gas-liquid mass transfer in absorption, chemical reactions and precipitation processes were investigated. The effects of particles on absorption mass transfer and the effects of operating conditions on gas-liquid reactive crystallization were detailed and comprehensively analyzed. The analysis gave insights into the interactive mechanisms of gas-liquid-solid three phase systems and offered new ideas and references for development of reactive crystallization processes. Moreover, Raman spectrometry was successfully applied for anti-solvent precipitation and evaporation crystallization. Raman analysis can provide real-time information for identification and quantification of crystal polymorphs. A solubility expression based on Pitzer theory was derived to support the research of anti-solvent crystallization. Based on the theoretical and experimental investigations in this study, the main findings are presented as below.

Firstly, the solubility of KCl in MgCl_2 -KCl- H_2O system was theoretically studied. The activity coefficient and solubility of KCl at 25 °C could be predicted by iteration method. The solubility of KDP in the binary solvents (water + acetone), (water + ethyl acetate) and (water + thiourea) at (298.15-313.15) K were determined experimentally. The solubility data derived fills a gap in the solubility database. The results showed that the solubility of KDP increases with temperature increase at constant composition of solvents, and decreases with increase in concentration of non-electrolytes at constant temperature. The relationship of temperature T and the Pitzer parameter λ refers to interaction between ions and non-electrolyte molecules obtained by the simplified Pitzer model. The developed Pitzer model can express well and determine accurately the solubility of KDP in non-electrolyte solutions. In the present work the derived Pitzer model is valid at molality of the non-electrolyte below 6 mol kg^{-1} . This is maybe a limitation for the established model. In future work, more systems should be studied to establish in more detail the applicability and predictive capability of this model.

Secondly, semi-batch precipitation of magnesium carbonate from the reaction of magnesium hydroxide and carbon dioxide was investigated. In the temperature range of 25 to 62 °C and at atmospheric pressure, crystalline magnesium carbonate trihydrate with needle-like shape was mainly obtained as crystalline product. The mean particle size was approximately 20 to 25 μm . Increase in temperature and pore size of the gas sparger promoted the formation of larger particles. Magnesium carbonate with smaller particles were precipitated at higher initial slurry concentration of $\text{Mg}(\text{OH})_2$. The results indicate that there is no effect of particle size of $\text{Mg}(\text{OH})_2$ on the particle size distribution of final precipitates at low flow rate of CO_2 . However, there is a remarkable effect at higher CO_2 flow rate. Moreover, kinetics information such as concentration of ions in the liquid phase and quantity of solids in the solid phase was captured and analyzed in the studied semi-batch reactive crystallization process. It can be concluded that mass transfer of CO_2 is a critical factor in control of the heterogeneous system. Stirring rate had an impact on the dissolution rate of $\text{Mg}(\text{OH})_2$, but this effect also depends on other factors such as gas flow

rate and suspension density. A mixing rate of 650 rpm was found to be the optimal speed for the configuration studied.

The models developed in this work on the basis of Raman spectrometry and thermal analysis method can determine the components in precipitated solid mixtures, which yields information on the dynamics of the reaction system and the consumption of reactant $\text{Mg}(\text{OH})_2$ and formation of magnesium carbonate. Furthermore, the agreement between these two models indicates that reaction kinetics could be monitored through Raman analysis of the solid phase. Inline measurements by Raman probe immersed in the crystallizer can collect information on kinetic phenomena in a fast and simple way. It should be pointed out that inline Raman analysis seems to have great potential for wide utilization in crystallization process studies.

The studied MgCO_3 precipitation system is complicated because solid particles exist throughout the whole process. Therefore, nucleation, crystal growth and aggregation/agglomeration rates cannot be investigated easily. However, crystal size distribution of the final product and the collected kinetic data of concentrations in the mother liquor and solid phase composition allow development of a modeling approach where these kinetic factors of precipitation can be obtained. In practice, development of carbonate method has great potential value in collecting and recycling magnesium sources from industrial wastewaters or mineral rocks and in capturing and storing CO_2 . Several kinds of flue gases containing CO_2 could be used as a reactant. Furthermore, the proposed carbonation precipitation process can be used to separate also other cations.

Thirdly, the effect of solid particles on absorption mass transfer was investigated at constant temperature and gas flow. As it can be expected, mass transfer was enhanced with increase in mixing intensity. No effect on mass transfer rate was found from the different sized quartz and fine calcium carbonate particles at low suspension density. However, k_La rose as the amount of fine calcium carbonate particles increased. The existence of small particles enhances renewal and movement of the interface, and hinders the coalescence of bubbles. Therefore, mass transfer rate becomes higher with increased small particle concentration. An empirical model describing the effect of solids on gas-liquid mass transfer was derived. The major factors were mixing input, solid content and liquid effective viscosity, whereas particle size had a minor effect on obtained volumetric mass transfer coefficient values. This observation reveals that the effect of the presence of solids on gas-liquid mass transfer cannot be ignored, especially when small particles exist in the system.

Finally, Raman spectrometry was successfully applied to anti-solvent precipitation of KDP in a mixed solvent of acetone and water. The supersaturation profiles of KDP were obtained by usage of a Raman immersion probe. The results showed that the feeding rate had a significant effect on precipitation. The feeding position, on the other hand, did not affect precipitation so much. Evaporation crystallization of IMC in organic solvent was also studied. Raman spectroscopy was easily able to identify the polymorph of precipitated IMC. Therefore, Raman spectrometry is clearly a powerful tool to investigate complicated crystallization processes. Inline Raman spectroscopy can result in real-time

information on the concentration of solute in the liquid phase and thus the supersaturation degree, which is the driving force in crystallization. In addition, other useful information regarding solid composition and formed polymorphs is provided. Nevertheless, an appropriate calibration model is essential for accurate quantification by Raman spectroscopy.

References

- Adiya D. P., Paul E. L., Mark S. K. (2001). Low-level determination of polymorph composition in physical mixtures by near-infrared reflectance spectroscopy. *Journal of Pharmaceutical Sciences*, 90(3), 360-370.
- Agarwal U. P., Reiner R. S., Ralph S. A. (2010). Cellulose I crystallinity determination using FT-Raman spectroscopy: Univariate and multivariate methods. *Cellulose*, 17(4), 721-733.
- Allan S. Myerson. (2002). *Handbook of Industrial Crystallization*. 2nd ed. Butterworth-Heinemann. United States of America.
- Alper, E., Wichtendahl, B., Deckwer, W. D. (1980). Gas absorption mechanism in catalytic slurry reactors. *Chem. Eng. Sci.*, 35, 217-222.
- Barata P. A., Serrano M. L. (1997). Thermodynamic representation of the solubility for potassium dihydrogen phosphate (KH_2PO_4) + water + alcohols system. *Fluid Phase Equilibria*, 141(1-2), 247-263.
- Botha A., Strydom C. A. (2001). Preparation of a magnesium hydroxyl carbonate from magnesium hydroxide. *Hydrometallurgy*, 62(3), 175-183.
- Brown C.J., Ni X. (2011). Online evaluation of paracetamol antisolvent crystallization growth rate with video imaging in an oscillatory baffled crystallizer. *Crystal Growth & Design*, 11, 719-725.
- Carteret C., Dandeu A., Moussaoui S., Muhr H., Humbert B., Plasari E. (2009). Polymorphism studied by lattice phonon Raman Spectroscopy and statistical mixture analysis method. Application to calcium carbonate polymorphs during batch crystallization. *Crystal Growth & Design*, 9(2), 807-812.
- Chapman C. M., Nienow A. W., Cooke M., Middleton J. C. (1983). Particle-gas-liquid mixing in stirred vessels, Part III: three-phase mixing. *Chemical Engineering Research and Design*, 61, 167-181.
- Chen P. C., Chen C. C., Fun M. H., Liao O. Y., Jiang J. J., Wang Y. S., Chen C. S. (2004). Mixing and crystallization kinetics in gas-liquid reactive crystallization. *Chemical Engineering & Technology*, 27(5), 519-528.
- Cheng W., Li Z. (2009). Precipitation of nesquehonite from homogeneous supersaturated solutions. *Cryst. Res. Technol.*, 44(9), 937-947.
- Cheng W., Li Z. (2010). Nucleation kinetics of nesquehonite ($\text{MgCO}_3 \cdot 3\text{H}_2\text{O}$) in the MgCl_2 - Na_2CO_3 system. *Journal of Crystal Growth*, 312, 1563-1571.
- Cooke M., Heggs P.J., Rodgers T.L. (2008). The effect of solids on the dense phase gas fraction and gas-liquid mass transfer at conditions close to the heterogeneous regime in a mechanically agitated vessel. *Chemical Engineering Research and Design*, 86, 869-882.
- Coulson J. M., Richardson J. F., Backhurst J. R., Harker J. H. (2002). *Chemical Engineering*, Vol. 2, 5th ed., *Particle Technology & Separation Processes*, UK: Butterworth-Heinemann, 239.
- Ding X. (1985). *Industry crystallization*. Chemical Industry Press, Beijing. (Chinese)
- Dong M., Cheng W., Li Z., Demopoulos P.G. (2008). Solubility and stability of nesquehonite ($\text{MgCO}_3 \cdot 3\text{H}_2\text{O}$) in NaCl, KCl, MgCl_2 , and NH_4Cl solutions. *J. Chem. Eng. Data*, 53, 2586-2593.

- Dong M., Li Z., Mi J., Demopoulos P.G. (2009). Solubility and stability of nesquehonite ($\text{MgCO}_3 \cdot 3\text{H}_2\text{O}$) in mixed $\text{NaCl}+\text{MgCl}_2$, $\text{NH}_4\text{Cl}+\text{MgCl}_2$, LiCl , and $\text{LiCl}+\text{MgCl}_2$ solutions. *J. Chem. Eng. Data*, 54, 3002-3007.
- Dylag M., Talaga J. (1994). Hydrodynamics of mechanical mixing in a three-phase liquid-gas-solid system. *International Chemical Engineering*, 34, 539-551.
- Falcon J. A., Berglund K. A. (2003). Monitoring of antisolvent addition crystallization with Raman spectroscopy. *Crystal Growth & Design*, 3(6), 947-952.
- Fuchs, R., Ryu D. Y., Humphrey, A. E. (1971). Effect of surface aeration on scale-up procedures for fermentation on processes. *Ind. Eng. Process Des. Develop.*, 10(2), 190-196.
- Gentile F., Oleschko H., Veverka P., Machoň V., Paglianti A., Bujalski W., Etchells III A. W., Nienow A. W. (2003). Some effects of particle wettability in agitated solid-gas-liquid systems: gas-liquid mass transfer and the dispersion of floating solids. *The Canadian Journal of Chemical Engineering*, 81, 581-587.
- Gómez-Díaz D., Navaza J. M. (2003). Mass transfer in a flat gas/liquid interface using non-Newtonian media. *Chemical Engineering & technology*, 26(10), 1068-1073.
- Gómez-Díaz D., Navaza J. M. (2005). Gas/liquid mass transfer in carbon dioxide-alkanes mixtures. *Chemical Engineering Journal*, 114, 131-137.
- Han B., Niemi H., Sha Z., Louhi-Kultanen M. (2011). Influence of solid particles on gas-liquid mass transfer in stirred tank. *18th International Symposium on Industrial Crystallization*, Zurich, Switzerland, 13-16, September.
- Han B., Niemi H., Sha Z., Louhi-Kultanen M. (2012). Precipitation of magnesium carbonate by a reaction of magnesium hydroxide and CO_2 . *19th International Workshop on Industrial Crystallization*, Tianjin, China, 7-9 September.
- Han B., Sha Z., Louhi-Kultanen M. (2014). Factors influencing the particle size distribution of magnesium carbonate trihydrate. *Journal of Tianjin University of Science & Technology*, 29(2), 45-49. (Chinese)
- Han B., Wang X., Sha Z., Tang N., Zhao L. (2009). Solubility prediction of potassium chloride in the system $\text{KCl}-\text{MgCl}_2-\text{H}_2\text{O}$. *Journal of Salt and Chemical Industry*, 38(4), 4-7, 12. (Chinese)
- Hatakka H., Alatalo H., Louhi-Kultanen M., Lassila I., Hægström E. (2010). Closed-loop control of reactive crystallization part II: Polymorphism control of L-glutamic acid by sonocrystallization and seeding. *Chemical Engineering & Technology*, 33(5), 751-756.
- Haynes W. (2012). *CRC Handbook of Chemistry and Physics*, 92nd ed., (Internet version).
- Hänchen M., Prigiobbe V., Baciocchi R., Mazzotti M. (2008). Precipitation in the Mg-carbonate system-effects of temperature and CO_2 pressure. *Chem. Eng. Sci.*, 63, 1012-1028.
- He M., Wang Y., Forssberg E. (2006). Parameter studies on the rheology of limestone slurries. *Int. J. Miner. Process*, 78, 63-77.
- Jiang L., Luo K., Li H. (2004). Study on the crystallization kinetics of potassium dihydrogen phosphate from wet-process phosphoric acid purified by crystallization of melamine phosphate, *Ind. Miner. Process.*, 33(6), 7-9.
- Jiao D., King C., Grossfield A., Darden T. A., Ren P. Y. (2006). Simulation of Ca^{2+} and Mg^{2+} solvation using polarizable atomic multipole potential. *The Journal of Physical Chemistry B*, 110(37), 18553-18559.

- Juárez P., Orejas J. (2001). Oxygen transfer in a stirred reactor in laboratory scale. *Latin American Applied Research*, 31, 433-439.
- Joshi M.S., Antony A.V. (1980). Kinetics of growth & dissolution of potassium dihydrogen phosphate crystal in aqueous solutions. *Indian J. Pure Appl. Phys.*, 18, 479-482.
- Jouyban A., Khoubnasabjafari M., Chan H., Clark B., Acree W. (2002). Solubility prediction of anthracene in mixed solvents using a minimum number of experimental data. *Chem. Pharm. Bull.*, 50(1), 21-25.
- Kielbus-Rapala A., Karcz J. (2009). Influence of suspended solid particles on gas-liquid mass transfer coefficient in a system stirred by double impeller. *Chemical Papers*, 63(2), 188-196.
- Kim Y., Haam S., Shul Y.G., Kim W., Jung J.K., Eun H., Koo K. (2003). Pseudopolymorphic crystallization of L-Ornithine-L-aspartate by drowning out. *Ind. Eng. Chem. Res.*, 42, 883-889.
- Kitamura M., Sugimoto M. (2003). Anti-solvent crystallization and transformation of thiazole derivative polymorphs-I: effect of addition rate and initial concentrations, *Journal of Crystal Growth*, 257, 177-184.
- Kluytmans J.H.J., van Wachem B.G.M., Kuster B.F.M., Schouten J.C. (2003). Mass transfer in sparged and stirred reactors: influence of carbon particles and electrolyte. *Chemical Engineering Science*, 58, 4719-4728.
- Kordač M., Linek V. (2006). Mechanism of enhanced gas absorption in presence of fine solid particles: Effect of molecular diffusivity on mass transfer coefficient in stirred cell. *Chem. Eng. Sci.* 61, 7125-7132.
- Kuramochi H., Osako M., Kida A., Nishimura K., Kawamoto K., Asakuma Y., Fukui K., Maeda K. (2005). Determination of ion-specific NRTL parameters for predicting phase equilibria in aqueous multielectrolyte solutions. *Industrial & Engineering Chemistry Research*, 44(9), 3289-3297.
- Lee J., Ashokkumar M., Kentish S. E. (2014). Influence of mixing and ultrasound frequency on antisolvent crystallization of sodium chloride. *Ultrasonics Sonochemistry*, 21, 60-68.
- Li J., Tekie Z., Mizan T. I., Morsi B. I. (1996). Gas-liquid mass transfer in a slurry reactor operating under olefinic polymerization process conditions. *Chemical Engineering Science*, 51(4), 549-559.
- Linek V., Kordač M., Soni M. (2008). Mechanism of gas absorption enhancement in presence of fine solid particles in mechanically agitated gas-liquid dispersion. Effect of molecular diffusivity. *Chemical Engineering Science*, 63(21), 5120-5128.
- Linek, V., Sinkule, J., Beneš, P. (1991). Critical assessment of gassing-in method for measuring k_{LA} in fermentors. *Biotechnol. Bioeng.* 38, 323-330.
- Linek, V., Vacek, V., Beneš, P. (1987). A critical review and experimental verification of the correct use of the dynamic method for the determination of oxygen transfer in aerated agitated vessels to water, electrolyte solution and viscous liquids. *Chem. Eng. J.* 34, 11-34.
- McCabe W. L., Smith J. C., Harriott P. (2005). *Unit Operations of Chemical Engineering*. McGraw-Hill, 7th ed, New York.

- Mena P., Ferreira A., Teixeira J.A., Rocha F. (2011). Effect of some solid properties on gas-liquid mass transfer in a bubble column. *Chemical Engineering and Processing*, 50, 181-188.
- Mitsuhashi K., Tagami N., Tanabe K., Ohkubo T., Sakai H., Koishi M., Abe M. (2005). Synthesis of microtubes with a surface of "house of cards" structure via needlelike particles and control of their pore size. *Langmuir*, 21, 3659-3663.
- Mostafa Nowee S., Abbas Ali, Romagnoli Jose A. (2008). Antisolvent crystallization: Model identification, experimental validation and dynamic simulation. *Chemical Engineering Science*, 63, 5457-5467.
- Moucha, T., Linek, V., Sinkule, J. (1995). Measurement of k_{La} in multiple impeller vessels with significant axial dispersion in both phases. *Trans IChemE*, 73, part A, 286-290.
- Mullin J. W. (2001). *Crystallization*. 4th Edition. Oxford: Butterworth-Heinemann.
- Mullin J. W., Amatavivadhana A. (1967). Growth kinetics of ammonium- and potassium-dihydrogen phosphate crystals. *J. Appl. Chem.*, 17, 151-156.
- Nagy Z. K., Fujiwara M., Braatz R.D. (2008). Modelling and control of combined cooling and antisolvent crystallization processes. *Journal of Process Control*, 18, 856-864.
- Nandi A. K., Kshirsagar A. S., Thanigaivelan U., Bhattacharyya S. C., Mandal A. K., Pandey R. K., Bhattacharya B. (2014). Process optimization for the gas-liquid heterogeneous reactive crystallization process involved in the preparation of the insensitive high explosive TATB. *Central European Journal of Energetic Materials*, 11(1), 31-57.
- Nienow A. W., Konno M., Bujalski W. (1986). Studies on three-phase mixing: A review and recent results. *Chemical Engineering Research and Design*, 64, 35-42.
- Niu Z., Cheng F., Li B., Chen X. (2001). *Salt-water system phase diagrams and applications*. Tianjin University Press, Tianjin. (Chinese)
- Oguz H., Brehm A., Deckwer W. D. (1987). Gas/liquid mass transfer in sparged agitated slurries. *Chem. Eng. Sci.* 42, 1815-1822.
- Ohkubo T., Suzuki S., Mitsuhashi K., Ogura T., Iwanaga S., Sakai H., Koishi M., Abe M. (2007). Preparation of petaloid microspheres of basic magnesium carbonate. *Langmuir*, 23, 5872-5874.
- One T., ter Horst J. H., Jansens P. J. (2004). Quantitative measurement of the polymorphic transformation of L-glutamic acid using in-situ Raman spectroscopy. *Crystal Growth & Design*, 4(3), 465-469.
- O'Grady D., Barrett M., Casey E., Glennon B. (2007). The effect of mixing on the metastable zone width and nucleation kinetics in the anti-solvent crystallization of benzoic acid. *Chemical Engineering Research and Design, Trans IChemE*, Part A, 85 (A7), 945-952.
- Partanen J., Enqvist Y., Louhi-Kultanen M., Kallas J. (2003). Activity coefficients of potassium dihydrogen phosphate in aqueous solutions at 25 °C and in aqueous mixtures of urea and this electrolyte in the temperature range 20-35 °C. *Zeitschrift für Physikalische Chemie*, 217(6), 723-738.
- Pinho S. P., Macedo E. A. (2002). Experimental measurement and modeling of KBr solubility in water, methanol, ethanol, and its binary mixed solvents at different temperatures. *Journal of Chemical Thermodynamics*. 34(3), 337-360.

- Pitzer S. K. (1973). Thermodynamics of electrolytes. I. Theoretical basis and general equations. *The Journal of Physical Chemistry*, 77(2), 268-277.
- Pitzer S. K., Mayorga G. (1973). Thermodynamics of electrolytes. II. Activity and osmotic coefficients for strong electrolytes with one or both ions univalent. *The Journal of Physical Chemistry*, 77(19), 2300-2308.
- Pitzer S. K. (1991). *Activity coefficients in electrolyte solutions*. 2nd ed., CRC Press, Boca Raton, FL.
- Purwins M., Weber A., Berwian P., Mller G., Hergert F., Jost S., Hock R. (2006). Kinetics of the reactive crystallization of CuInSe₂ and CuGaSe₂ chalcopyrite films for solar cell applications. *Journal of Crystal Growth*, 287, 408-413.
- Rewatkar V. B., Raghava Rao K. S. M. S., Joshi J. B. (1991). Critical impeller speed for solid suspension in mechanically agitated three-phase reactors. 1. Experimental part. *Industry and Engineering Chemistry Research*, 30(8), 1770-1784.
- Ruthiya K. C., Kuster B. F. M., Schouten J. C. (2003a). Gas-liquid mass transfer enhancement in a surface aeration stirred slurry reactors. *The Canadian Journal of Chemical Engineering*, 81(3-4), 632-639.
- Ruthiya K. C., van der Schaaf J., Kuster B. F. M., Schouten J. C. (2003b). Mechanism of physical and reaction enhancement of mass transfer in a gas inducing stirred slurry reactor. *Chemical Engineering Journal*, 96(1-3), 55-69.
- Saleemi A.N., Rielly C.D., Nagy Z.K. (2012). Monitoring of the combined cooling and antisolvent crystallization of mixtures of aminobenzoic acid isomers using ATR. UV/vis spectroscopy and FBRM. *Chemical Engineering Science*, 77, 122-129.
- Sha Z., Han B., Louhi-Kultanen M. (2015). Influence of solid particles on gas-liquid mass transfer in a stirred tank. *Journal of Tianjin University of Science & Technology*, accepted. (Chinese)
- Shao P., Li Z., Mi J. (2009). Composition and morphology of magnesium carbonate hydrates synthesized by the reaction of MgSO₄ with Na₂CO₃ in 283~363 K. *The Chinese Journal of Process Engineering*, 9(3), 520-525.
- Smith J. M. (1990). Industrial needs for mixing research. *Chemical Engineering Research and Design*, 68(1), 3-6.
- Smith J. M., van't Riet K., Middleton J. C. (1977). Proc. 2nd Eur. Cof. On mixing, St. John's College, Cambridge, *BHIRA Fluid Eng.* Cranfield, England, F4-51.
- Stankiewicz A. (2003). Reactive separations for process intensification: an industrial perspective. *Chemical Engineering and processing*, 42, 137-144.
- Stenberg O., Andersson B. (1988). Gas-liquid mass transfer in agitated vessels-II. Modelling of gas-liquid mass transfer. *Chem. Eng. Sci.* 43(3), 725-730.
- Sudduth R. D. (2008). A new approach to controlling the viscosity of a coating with a blend of particles with significantly different shapes. *Pigment & Resin Technology*, 37(6), 362-374.
- Sun Y. Z., Song X. F., Jin M. M., Jin W., Yu J. G. (2013). Gas-liquid reactive crystallization of lithium carbonate by a falling film column. *Industrial & Engineering Chemistry Research*, 52, 17598-17606.
- Takiyama H., Otsuhata T., Matsuoka M. (1998). Morphology of NaCl crystals in drowning-out precipitation operation. *Chemical Engineering Research and Design*, 76 (A7), 809-814.

- Teir S., Eloneva S., Fogelholm C., Zevenhoven R. (2009). Fixation of carbon dioxide by producing hydromagnesite from serpentinite. *Applied Energy*, 86, 214-218.
- Teir S., Kuusik R., Fogelholm C., Zevenhoven R. (2007). Production of magnesium carbonates from serpentinite for long-term storage of CO₂. *Int. J. Miner. Process.*, 85, 1-15.
- Tosheva L., Valtchev V. (2005). Nanocerolites: Synthesis, crystallization mechanism, and applications. *Chem. Mater.* 17, 2494-2513.
- Vandu, C. O., Krishna, R. (2004). Influence of scale on the volumetric mass transfer coefficients in bubble columns. *Chemical Engineering and Processing*, 43, 575-579.
- Van't Riet K. (1979). Review of measuring methods and results in non-viscous gas-liquid mass transfer in stirred vessels. *Ind. Eng. Chem. Process Des. Dev.*, 18(3), 357-364.
- Varma S., Chen P. C., Unnikrishnan G. (2011). Gas-liquid reactive crystallization for the synthesis of CaCO₃ nanocrystals. *Materials Chemistry and Physics*, 126, 232-236.
- Velts O., Hautaniemi M., Uibu M., Kallas J., Kuusik R. (2010). Modeling of CO₂ mass transfer and hydrodynamics in a semi-batch reactor. *Journal of International Scientific Publication: Materials, Methods & Technologies*, 4(Part 2), 68-79.
- Wang Y., Li Z., Demopoulos P.G. (2008). Controlled precipitation of nesquehonite (MgCO₃·3H₂O) by the reaction of MgCl₂ with (NH₄)₂CO₃. *Journal of Crystal Growth*, 310, 1220-1227.
- Willoughby D. B., Sharma S. (2004). Coating talc does not have to have poor rheology. *TAPPI J.*, 3(8), 25-31.
- Wong C. W., Wang J. P., Haung S. T. (1987). Investigations of fluid dynamics in mechanically stirred aerated slurry reactors. *The Canadian Journal of Chemical Engineering*, 65(3), 412-419.
- Wu H. (1995). An issue on application of a disk turbine for gas-liquid mass transfer. *Chem. Eng. Sci.*, 50, 2801-2811.
- Yu Z., Chow P., Tan R. (2006). Seeding and constant-supersaturation control by ATR-FTIR in anti-solvent crystallization. *Organic Process Research & Development*, 10, 717-722.
- Yu Z. Q., Tan R.B.H., Chow P.S. (2005). Effects of operating conditions on agglomeration and habit of paracetamol crystals in anti-solvent crystallization. *Journal of Crystal Growth*, 279, 477-488.
- Yuan J., Murray H. H. (1997). The importance of crystal morphology on the viscosity of concentrated suspensions of kaolins. *Applied Clay Science*, 12, 209-219.
- Zhang J., Duan Z., Xu C., Zhou M. (2008). Solid effects on gas-liquid mass transfer in catalytic slurry system of isobutene hydration over fine ion exchange resin particles. *Chem. Eng. J.*, 136, 276-281.
- Zhang J., Xu C., Zhou M. (2006). The mechanism model of gas-liquid mass transfer enhancement by fine catalyst particles. *Chem. Eng. J.*, 120, 149-156.
- Zhang C., Wang H., Wang Y. (2010). Internally generated seeding policy in anti-solvent crystallization of ceftriaxone sodium. *Chemical Engineering and Processing: Process Intensification*, 49(4), 396-401.

- Zhang Y., Jiang Y., Zhang D., Li K., Qian Y. (2011). On-line concentration measurement for anti-solvent crystallization of β -artemether using UV-vis fiber spectroscopy. *Journal of Crystal Growth*, 314, 185-189.
- Zlokarnik M. (2001). *Stirring: Theory and practice*. Wiley-VCH, Weinheim.
- Zwietering T. N. (1958). Suspending of solid particals in liquid by agitators. *Chemical Engineering Science*, 8(3-4), 244-253.

Appendix A

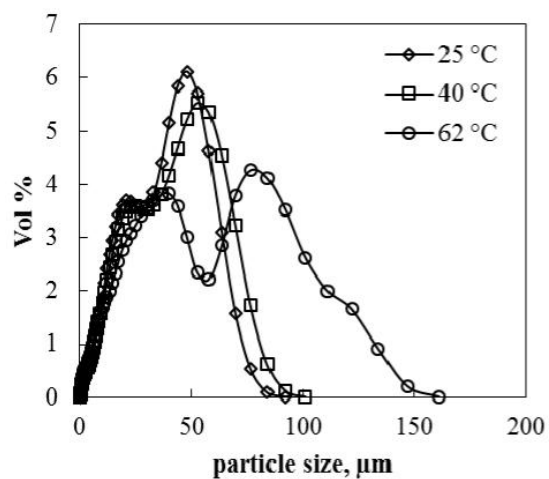


Fig. A1 Effect of temperature on crystal size distribution of the final product. (Fig. 2 in Han et al. 2014)

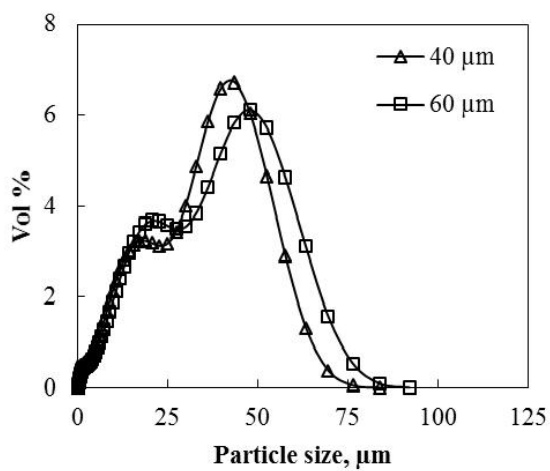


Fig. A2 Effect of pore size of sparger on the particle size distribution of the final product. (Fig. 3 in Han et al. 2014)

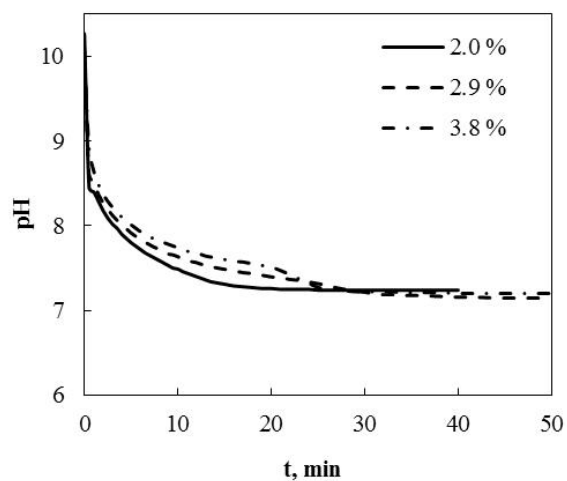


Fig. A3 Effect of the initial slurry concentration of magnesium hydroxide on pH. (Fig. 4 in Han et al. 2014)

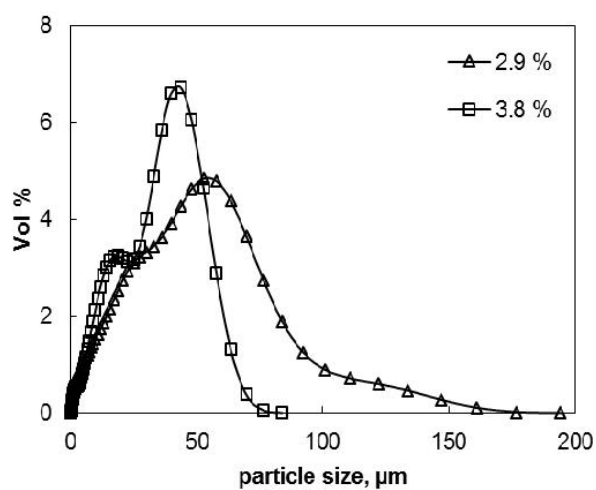


Fig. A4 Effect of initial slurry concentration of magnesium hydroxide on the particle size distribution of the product. (Fig. 5 in Han et al. 2014)

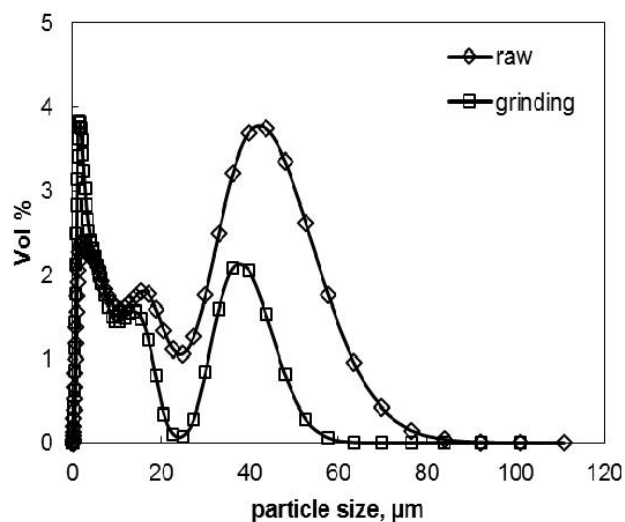


Fig. A5 Crystal size distribution of raw and milled magnesium hydroxide. (Fig. 6 in Han et al. 2014)

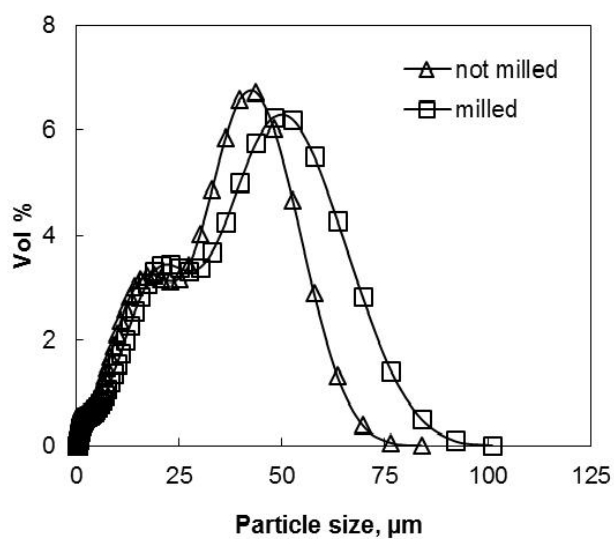


Fig. A6 Effect of the initial particle size of magnesium hydroxide on the particle size distribution of the final product at a flow rate of 9 L/min. (Fig. 7 in Han et al. 2014)

PART II: Publications

ACTA UNIVERSITATIS LAPPEENRANTAENSIS

- 608. HÄMÄLÄINEN, KIMMO. Improving the usability of extruded wood-plastic composites by using modification technology. 2014. Diss.
- 609. PIRTTILÄ, MIIA. The cycle times of working capital: financial value chain analysis method. 2014. Diss.
- 610. SUIKKANEN, HEIKKI. Application and development of numerical methods for the modelling of innovative gas cooled fission reactors. 2014. Diss.
- 611. LI, MING. Stiffness based trajectory planning and feedforward based vibration suppression control of parallel robot machines. 2014. Diss.
- 612. KOKKONEN, KIRSI. From entrepreneurial opportunities to successful business networks – evidence from bioenergy. 2014. Diss.
- 613. MAIJANEN-KYLÄHEIKO, PÄIVI. Pursuit of change versus organizational inertia: a study on strategic renewal in the Finnish broadcasting company. 2014. Diss.
- 614. MBALAWATA, ISAMBI SAILON. Adaptive Markov chain Monte Carlo and Bayesian filtering for state space models. 2014. Diss.
- 615. UUSITALO, ANTTI. Working fluid selection and design of small-scale waste heat recovery systems based on organic rankine cycles. 2014. Diss.
- 616. METSO, SARI. A multimethod examination of contributors to successful on-the-job learning of vocational students. 2014. Diss.
- 617. SIITONEN, JANI. Advanced analysis and design methods for preparative chromatographic separation processes. 2014. Diss.
- 618. VIHAVAINEN, JUHANI. VVER-440 thermal hydraulics as computer code validation challenge. 2014. Diss.
- 619. AHONEN, PASI. Between memory and strategy: media discourse analysis of an industrial shutdown. 2014. Diss.
- 620. MWANGA, GASPER GODSON. Mathematical modeling and optimal control of malaria. 2014. Diss.
- 621. PELTOLA, PETTERI. Analysis and modelling of chemical looping combustion process with and without oxygen uncoupling. 2014. Diss.
- 622. NISKANEN, VILLE. Radio-frequency-based measurement methods for bearing current analysis in induction motors. 2014. Diss.
- 623. HYVÄRINEN, MARKO. Ultraviolet light protection and weathering properties of wood-polypropylene composites. 2014. Diss.
- 624. RANTANEN, NOORA. The family as a collective owner – identifying performance factors in listed companies. 2014. Diss.
- 625. VÄNSKÄ, MIKKO. Defining the keyhole modes – the effects on the molten pool behavior and the weld geometry in high power laser welding of stainless steels. 2014. Diss.

626. KORPELA, KARI. Value of information logistics integration in digital business ecosystem. 2014. Diss.
627. GRUDINSCHI, DANIELA. Strategic management of value networks: how to create value in cross-sector collaboration and partnerships. 2014. Diss.
628. SKLYAROVA, ANASTASIA. Hyperfine interactions in the new Fe-based superconducting structures and related magnetic phases. 2015. Diss.
629. SEMKEN, R. SCOTT. Lightweight, liquid-cooled, direct-drive generator for high-power wind turbines: motivation, concept, and performance. 2015. Diss.
630. LUOSTARINEN, LAURI. Novel virtual environment and real-time simulation based methods for improving life-cycle efficiency of non-road mobile machinery. 2015. Diss.
631. ERKKILÄ, ANNA-LEENA. Hygro-elasto-plastic behavior of planar orthotropic material. 2015. Diss.
632. KOLOSENI, DAVID. Differential evolution based classification with pool of distances and aggregation operators. 2015. Diss.
633. KARVONEN, VESA. Identification of characteristics for successful university-company partnership development. 2015. Diss.
634. KIVYIRO, PENDO. Foreign direct investment, clean development mechanism, and environmental management: a case of Sub-Saharan Africa. 2015. Diss.
635. SANKALA, ARTO. Modular double-cascade converter. 2015. Diss.
636. NIKOLAEVA, MARINA. Improving the fire retardancy of extruded/coextruded wood-plastic composites. 2015. Diss.
637. ABDEL WAHED, MAHMOUD. Geochemistry and water quality of Lake Qarun, Egypt. 2015. Diss.
638. PETROV, ILYA. Cost reduction of permanent magnet synchronous machines. 2015. Diss.
639. ZHANG, YUNFAN. Modification of photocatalyst with enhanced photocatalytic activity for water treatment. 2015. Diss.
640. RATAVA, JUHO. Modelling cutting states in rough turning of 34CrNiMo6 steel. 2015. Diss.
641. MAYDANNIK, PHILIPP. Roll-to-roll atomic layer deposition process for flexible electronics applications. 2015. Diss.
642. SETH, FRANK. Empirical studies on software quality construction: Exploring human factors and organizational influences. 2015. Diss.
643. SMITH, AARON. New methods for controlling twin configurations and characterizing twin boundaries in 5M Ni-Mn-Ga for the development of applications. 2015. Diss.
644. NIKKU, MARKKU. Three-dimensional modeling of biomass fuel flow in a circulating fluidized bed furnace. 2015. Diss.
645. HENTTU, VILLE. Improving cost-efficiency and reducing environmental impacts of intermodal transportation with dry port concept – major rail transport corridor in Baltic Sea region. 2015. Diss.

